Geothermics 136 (2026) 103552

Contents lists available at ScienceDirect

Geothermics

journal homepage: www.elsevier.com/locate/geothermics

Geothermal potential of karstified Devonian carbonates in NW Germany

Manfred Heinelt [a,b,c,*], Mathias Mueller [b], Benedikt Ahrens [c,a], Mathias Nehler [a], Katharina Alms [a,d], Adrian Immenhauser [b,a]

[a] Fraunhofer IEG, Fraunhofer Research Institution for Energy Infrastructures and Geotechnologies IEG, Am Hochschulcampus 1/IEG, 44801 Bochum, Germany
[b] Institute of Geosciences, Faculty for Geography and Geosciences, Ruhr-University Bochum, Universitätsstrasse 150, 44801 Bochum, Germany
[c] Wissenschaftsbereich Georessourcen und Verfahrenstechnik, Technische Hochschule Georg Agricola, Herner Str. 45, 44787 Bochum, Germany
[d] Geothermal Energy Systems, Ruhr-University Bochum, Universitätsstrasse 150, 44801 Bochum, Germany

ARTICLE INFO

Keywords:
Carbonate
Limestone
Geothermal reservoir
Karst system
Permeability

ABSTRACT

The exploration of suitable reservoir rocks for deep geothermal energy in NW Germany focuses on karstified carbonates of Carboniferous and Devonian age. Using a case example from the city of Iserlohn, we demonstrate that these rocks exhibit high thermal yields due to the secondary porosity caused by meteoric (and potentially hypogenic) karstification. Karstified carbonates, if structurally interconnected on a reservoir scale, have the potential to provide significantly higher permeability. We conducted thermo-triaxial cell experiments for depths exceeding 2 km. Our findings indicate that dolostones offer enhanced mechanical integrity and exhibit reduced porosity loss with increasing depth. Visual inspections of μCT scans confirm that karstification results in large, interconnected pores that have been leached. The effective porosity of karstified carbonates reaches 14 %, with measured permeability values in the order of 10^{-16} m^2. In terms of porosity and permeability, karstified units can outperform non-karstified ones by up to two orders of magnitude. We conducted heat-in-place modelling using petrophysical laboratory data as input parameters for Monte Carlo simulations. An initial map was created to illustrate the potential geothermal energy stored and to identify areas with the highest energy yield. The estimated potential energy stored in the subsurface is greatest in the southern part of the Iserlohn study area, where the thickness of the Devonian carbonates is at its maximum. This deeper occurrence in the subsurface leads to a significant increase in reservoir temperature. The modelling results indicate a potential energy range for the entire distribution of Devonian carbonates between 87 TJ (P90) and 110 TJ (P10).

1. Introduction

Globally, limestone and dolostone aquifers play a crucial role in thermal water supply, second only to volcanic lithologies (Goldscheider et al., 2010). The suitability of subsurface carbonate rock bodies as geothermal reservoirs for hydrothermal applications is primarily controlled by their porosity and permeability. High permeability is essential for achieving an economically viable hydrothermal system, as it ensures sufficient fluid flow in addition to favourable subsurface temperatures (Limberger et al., 2018). Unlike clastic reservoirs, which typically exhibit high primary porosity and permeability properties, massive carbonate aquifers undergo rapid destruction of matrix porosity and permeability during burial diagenesis (compaction, dewatering, dissolution). In many cases, enhanced permeabilities in carbonates primarily result from processes in the burial realm or during uplift. The processes involved include, for example, carbonate leaching and dissolution as well as neomorphism or fracturing (Fryar, 2021; Lippert et al., 2022; Fritzer et al., 2022; Immenhauser, 2022). This pattern is particularly relevant because geothermal reservoirs for hydrothermal heat generation require well-connected pore systems, fracture networks and dissolution (e.g., meteoric and hypogenic karst) cavities to facilitate fluid migration and thermal exchange (Hölting and Coldewey, 2013). In particular, meteoric karstification — the dissolution of carbonate rocks by means of meteoric waters and soil zone CO_2 (Land, 1970; James and Choquette, 1990) — can create highly interconnected pore networks, and this substantially enhances permeability and heat storage capacity (Stober and Bucher, 2021), transforming previously impermeable formations into productive geothermal reservoirs (Homuth et al., 2015).

Despite the commonly observed destruction of primary porosity during burial, numerous Palaeozoic carbonate formations in Europe sustain substantial thermal water flow and may serve as viable geothermal reservoirs due to various diagenetic processes during burial

* Corresponding author.
E-mail address: manfred.heinelt@ieg.fraunhofer.de (M. Heinelt).

https://doi.org/10.1016/j.geothermics.2025.103552
Received 3 August 2025; Received in revised form 21 November 2025; Accepted 27 November 2025
Available online 8 December 2025

and fracturing in the context of structural overprint (Burs et al., 2016; Blöcher et al., 2019; Lippert et al., 2022). Prominent examples include the karstified Triassic carbonates of Hungary, which host Europe's largest thermal spring, and the Stuttgart thermal water system, sourced from Middle Triassic Muschelkalk limestones (Ufrecht, 2006; Goldscheider et al., 2010). In Germany, deep-seated geothermal systems are particularly well-documented in Southern Germany, including the Unterhaching geothermal project near Munich. There, Upper Jurassic (Malm) limestones serve as high-yield geothermal reservoirs at depths of up to 5,000 m, and geothermal waters reach temperatures of 165 °C (Goldscheider et al., 2010; Dirner and Steiner, 2015). Depending on geological conditions and system configuration, geothermal heat can be efficiently utilised for district heating applications at temperatures as low as 60 °C. The heat is typically extracted from depths exceeding 1, 000 m (Agemar et al., 2011; Stober and Bucher, 2021).

However, unlike southern Germany, the development of deep geothermal projects is currently limited in North Rhine-Westphalia (Western Germany), where Carboniferous and Devonian carbonates are present at depths ranging from several hundred to several thousand meters (Krebs, 1974; Lippert et al., 2022). Among these Palaeozoic carbonate units, the Devonian strata are considered among the most promising geothermal targets for hydrothermal heat production due to their widespread subsurface distribution, substantial stratigraphic thickness (up to 1.3 km), and burial depths exceeding 4 km beneath the Ruhr area in North Rhine-Westphalia (Balcewicz et al., 2021; Lippert et al., 2022). Accordingly, geothermal exploration efforts in North Rhine-Westphalia primarily focused on limestones and dolostones assigned to the Carboniferous and Devonian epochs, as these stratigraphic units exhibit the most favourable petrophysical characteristics for deep hydrothermal exploitation (Arndt, 2021; Fritschle et al., 2021; Lippert et al., 2022; Heinelt et al., 2025; Mueller et al., 2025). However, due to the inherent heterogeneity of karstified and fractured carbonates, permeability is also one of the most difficult parameters to evaluate, especially in the early exploration stages (Cross and Burchette, 2025).

Previous studies have assessed the geothermal potential of Devonian and Carboniferous carbonates in North Rhine-Westphalia by evaluating fracture networks, diagenetic alteration (predominantly dolomitisation) and meteoric and hypogenic (Immenhauser and Rameil, 2011) karstification (Balcewicz et al., 2021; Pederson et al., 2021; Fritschle et al., 2021; Lippert et al., 2022; Mueller et al., 2023, 2024, 2025; Jagert et al., 2025; Uwakwe et al., 2025). The geothermal potential of Lower Carboniferous and Middle to Upper Devonian (Massenkalk) carbonates is evaluated within the context of the Weisweiler project as part of efforts to transition district heating systems from fossil fuel dependence to sustainable geothermal sources (Fritschle et al., 2021). While studies on the geothermal potential of Devonian carbonates in the Right Rhenish Slate Mountains remain scarce, recent research has focused on fracture networks in quarries along the northern Remscheid-Altena anticline (Balcewicz et al., 2021).

Exploration efforts include the investigation of Devonian carbonate rocks in the Hagen-Hohenlimburg region, with the goal of utilising geothermal heat for industrial applications. For instance, a local paper mill (Kabel Pulp & Premium GmbH) has explored the potential for deep geothermal energy to reduce its natural gas consumption by 50 %, thereby decreasing annual CO_2 emissions by 30,000 tons (Lippert et al., 2022). Lippert et al. (2022) analysed the petrophysical and mineralogical properties of Devonian carbonates in North Rhine-Westphalia to assess their reservoir potential. Meanwhile, Mueller et al. (2024) explored the diagenetic history of Devonian carbonates at Steltenberg Quarry (Hagen-Hohenlimburg), reconstructing both hypogenic (hydrothermal) and meteoric karstification phases. Along similar lines, the Devonian carbonate rocks in the Iserlohn area are known for their extensive meteoric karst systems, which host over 100 caves formed through a complex series of leaching and dissolution processes (Niggemann et al., 2008; Immenhauser et al., 2023). Given the widespread regional occurrence of these karst features, it seems that similar structures may also be present at reservoir depths, where they overprint existing structural and diagenetic pathways, similar to those in the Jurassic host rocks of the Munich area in southern Germany (Hörbrand et al., 2025). That said, it seems clear that meteoric karstification has the potential to enhance permeability and create favourable conditions for hydrothermal heat exploitation. Nevertheless, the authors realise that meteoric karstification is but one of the karst mechanisms relevant in this context—particularly the aspect of hypogenic karsting, related to corrosive fluids at depth (Immenhauser et al., 2007; Klimchouk et al., 2017), deserves attention.

Considering the above aspects, this study focuses on karstified Devonian carbonate units located near Iserlohn, a city located approximately 25 km southeast of Dortmund in the Ruhr area, North Rhine-Westphalia (Fig 1). The investigation seeks to elucidate the influence of meteoric karstification on porosity, permeability and subsurface fluid flow pathways. In parallel, it evaluates the extent to which laboratory-derived petrophysical properties reflect the hydraulic and thermal potential of deep-seated karstified carbonates. We explore how variations in porosity, bulk density and specific heat capacity affect the estimated heat-in-place of both potentially karstified and consolidated carbonate reservoirs. The outcome of this work aims to establish an integrated methodological framework for characterising geologically, diagenetically and petrophysically complex carbonate systems, providing transferable insights for geothermal exploration in analogous lithologies elsewhere.

2. Geological setting

The study area, situated in North Rhine-Westphalia, is located within the Rhenohercynian Zone of the Central European Variscan Mountains. This zone originated as a passive continental margin that later evolved into a foreland basin due to the late Palaeozoic convergence of Gondwana and Laurussia (Oncken, 1988). During the Early to Middle Devonian, sediment deposition in this region was dominated by shallow marine to deltaic siliciclastic environments, controlled by crustal thinning along the southern margin of the Old Red Continent (Krebs, 1974; Oncken, 1988). This extensional regime facilitated the formation of the Rhenohercynian Basin, a shelf sea that gradually transitioned to carbonate sedimentation in the Upper Middle Devonian (Givetian, ca 388 Ma; Krebs, 1974; Grabert, 1998). The Devonian carbonate successions in North Rhine-Westphalia have been the subject of extensive stratigraphic and facies studies. Early investigations by Paeckelmann (1922) provided a first stratigraphic framework, while Krebs (1967, 1968, 1974) conducted comprehensive facies analyses despite the challenges posed by limited outcrop exposure. More recent studies by Stichling et al. (2022) and Löw et al. (2022) have further refined the lithostratigraphic classification of these units.

Extensive carbonate deposition in what is today the Iserlohn/Hagen-Hohenlimburg area (Fig 1) resulted in thick limestone successions referred to as Massenkalk (correspondingly translated as "Massive Limestones"), which are part of the Hagen-Balve Reef Complex and reach thicknesses of approximately 450 to 700 m (Niggemann et al., 2008; Becker et al., 2016). The carbonate factory remained active until the early Late Devonian (Frasnian), after which siliciclastic influx once again became dominant (Krebs, 1974). Following deposition, the Devonian carbonates underwent significant post-sedimentary alteration. The late Palaeozoic Variscan Orogeny (Carboniferous–Permian) was characterised by intense folding and faulting, accompanied by hydrothermal fluid circulation that led to dolomitisation and mineralisation (Gillhaus et al., 2003). The Devonian carbonates of the northern part of the Rhenish Massif, in the vicinity of the study area, were buried to a maximum depth of approximately 6.5 km during the later stages of the Variscan Orogeny, around 300 million years ago. Since the Permian (Zechstein), the Palaeozoic pre- and syn-Variscan sediments of the region have experienced an uplift and subsequent cooling process. Concurrently, the overburden thicknesses within the study area have

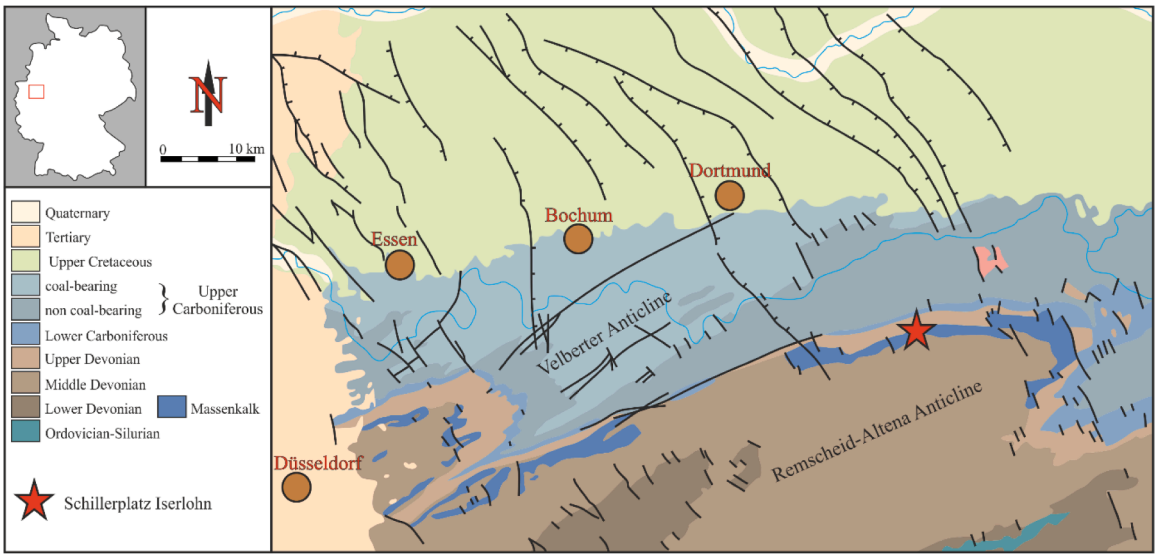

Fig. 1. Geological map of the northern Rhenish Massif. Red asterisk indicates the Schillerplatz in Iserlohn (modified after Pederson et al., 2021; Götte, 2004).

been eroded to a thickness ranging from 4 to 5.5 km (Littke et al., 2000; Nöth et al., 2001; Götte, 2004). Karstification of the Devonian carbonate units is a well-documented phenomenon, and the region features numerous cave systems (Niggemann et al., 2008 and references therein; Immenhauser et al., 2023). The majority of these were found to be the result of tectonically induced hydrothermal activity (Mesozoic-Cenozoic) and/or meteoric phreatic (Oligocene-Recent) processes (Niggemann et al., 2008; Drozdzewski et al., 2017; Richter et al., 2020). These processes played a crucial role in modifying the petrophysical properties of the carbonate rock bodies by enhancing secondary porosity and permeability (Becker et al., 2016). Near-surface meteoric karstification in the Devonian limestones of North Rhine-Westphalia is well-documented, and dissolution features have been shown to extend to depths of several hundred meters or more (Köhler, 1990).

The Hagen-Balve Reef Complex was recently reclassified, revealing two distinct members in the Iserlohn area. The lower unit, the Binolen Member, corresponds to the Schwelm facies described by Krebs (1974) and consists of dark grey, dense limestones containing abundant reef-building organisms such as corals, stromatoporoids, and crinoidal debris (Krebs, 1974; Löw et al., 2022; Stichling et al., 2022). Overlying this, the Asbeck Member represents the primary reef-building phase (Dorp facies; Krebs, 1974) and is characterised by a well-developed biohermal reef framework (Stichling et al., 2022). The samples studied and described here originate from the extensive Devonian limestone succession of the Hagen-Balve Reef Complex, which underlies the urban area of Iserlohn (Fig 1).

3. Study site and methodology

To evaluate the hydrothermal reservoir potential of Devonian carbonates with a focus on karstification, three drill cores from Schillerplatz, Iserlohn (BK-6/DABO_325,824: E 3409,660, N 5692,040; BK-9/DABO_325,825: E 3409,762, N 5694,236; BK-11/DABO_325,826: E 3409,785, N 5694,172), were systematically logged and classified according to Dunham (1962) and Embry and Klovan (1971) to establish the depositional framework. The lithological description followed the carbonate classification scheme of Flügel (2010), with a particular emphasis on dolomitisation. Based on core inspection, representative samples were selected for petrographic and petrophysical analyses. Petrographic investigations were conducted on thin sections, while petrophysical rock properties were determined from cylindrical core plugs. The resulting petrophysical dataset was subsequently incorporated into a volumetric heat-in-place model to quantify the geothermal energy potential of the studied carbonate succession.

3.1. Facies analysis and cement petrography

Petrographic analyses focused on characterising depositional facies, diagenetic overprinting, and cement stratigraphy. A total of 26 thin sections were prepared from macroscopically distinguishable rock samples, covering all volumetrically relevant facies types in the study area. The mineralogical composition was determined via X-ray diffraction (XRD) to differentiate between calcite and dolomite-dominated carbonate units. Measurements were conducted on a PANAlytical X'Pert Powder diffractometer in Bragg-Brentano geometry using a CuKα radiation source ($\lambda = 0.154$ nm) at 45 kV and 40 mA, over a 2Θ range of 5–100° with a step size of 0.0131° Particular emphasis was placed on porous and karstified intervals to evaluate the influence of secondary porosity on reservoir properties.

Facies classification was based on fossil assemblages, allochem composition, and porosity characteristics. Eleven thin sections were stained with *Alizarin Red S* to distinguish calcite from dolomite, following the methodology of Coniglio et al. (2004). In this procedure, non-ferruginous calcite appears red to pink, ferruginous calcite exhibits blue to purple hues, and unstained regions correspond to non-ferruginous dolomite or non-carbonate minerals. Thin sections were examined using a Zeiss Axio Scope A1 polarising microscope, and digital images were captured at a resolution of 2400 × 1800 pixels to document primary depositional features and early diagenetic modifications.

The cement paragenesis and, based on this, the deconvolution of the diagenetic history of these rocks was further investigated using cathodoluminescence microscopy to discern cement phases and overprinting relationships. Polished thin sections were analysed with a Lumic HC8-LM hot cathode cathodoluminescence microscope at Ruhr-University Bochum, equipped with an Olympus DP73 camera system. Thin sections were carbon-coated to ensure conductivity, and cathodoluminescence analyses were performed at an acceleration voltage of 14 kV with a beam current of 0.1 to 0.3 mA, following Neuser et al. (1995). The luminescence properties of calcite and dolomite cements were evaluated to differentiate diagenetic phases, guided by the classification schemes of Marshall (1988) and Burley (1978). The terminology used for dolomite follows Sibley and Gregg (1987). The paragenetic succession of Devonian carbonates follows the terminology from Mueller et al. (2024).

3.2. Experimental petrophysical analysis

Petrophysical parameters such as porosity, thermal conductivity, specific heat capacity, and permeability play a significant role in determining reservoir potential (Stober and Bucher, 2021). In particular, permeability is a key parameter for reservoir characterisation. However, at the early stages of exploration in carbonate reservoirs, permeability is one of the most challenging parameters to investigate at an appropriate scale (Cross and Burchette, 2025). To achieve a hydrothermal deep geothermal system, a high permeability of the reservoir rock is required in addition to a suitable reservoir temperature in the subsurface (Limberger et al., 2018). Naturally, high permeabilities can occur due to fractures or karstification (Lippert et al., 2022; Fritzer et al., 2022).

Nine cylindrical samples, each with a diameter of 40 mm, were extracted from several cores drilled in the Schillerplatz Iserlohn location using diamond-edged hollow drill bits. These cores were then precisely cut and ground to a final length of 80 mm using diamond-coated polishing discs to ensure parallel end faces (cf., Koelen et al., 2021). Water served as a coolant during the preparation process. Following oven drying at 60 °C for 48 h, the petrophysical properties of all samples were assessed under ambient conditions and for selected samples at simulated reservoir conditions.

3.2.1. Ambient conditions

Bulk density (ρ_{dry}) was determined by measuring the geometric dimensions (i.e., sample volume V) and masses of the cylindrical samples in both dry and saturated states. Grain density (ρ_{grain}) was obtained through pycnometer analysis. For this, finely powdered rock samples were used to eliminate the influence of pore spaces, following the DIN (18124:2019-02)standard. To ensure the accuracy of grain density measurements and eliminate the influence of pore spaces, the remaining material from sample preparation was processed into ultra-fine powder (<125 µm). This was achieved by initially crushing the material using a jaw crusher, followed by further refinement in a ball mill to attain the desired granularity. The analysis employed Gay-Lussac pycnometers with volumes of 25.0827 cm^3 and 25.1262 cm^3 to ensure precise measurements.

To assess the impact of pore spaces on the geothermal reservoir potential of the carbonate samples, both total porosity and effective porosity were quantified. Total porosity encompasses all voids within a porous material, whereas effective porosity accounts only for the interconnected pore volume, which is critical for fluid flow and storage. Total porosity (ϕ_{tot}) was calculated using the formula:

$$\phi_{tot} = 100 \cdot \left(1 - \frac{\rho_{dry}}{\rho_{grain}}\right). \quad (1)$$

Effective porosity, or connected porosity, was derived from the mass difference between the dry (m_{dry}) and water-saturated (m_{sat}) states. Water saturation was established following a vacuum saturation procedure with distilled water in a desiccator. Effective porosity (ϕ_{eff}) was calculated as follows

$$\phi_{eff} = \frac{m_{sat} - m_{dry}}{\rho_{wt} \cdot V}, \quad (2)$$

where ρ_{wt} denotes the density of water at ambient conditions (Manger, 1963). In karstified or fractured samples, particularly when large vuggy cavities occurred near the sample surface, water could drain from these features upon removal from the desiccator prior to weighing. Consequently, the laboratory-determined effective porosity may underestimate the true connected porosity of the specimen, and the actual effective porosity is likely higher than indicated by the measurement.

Three-dimensional datasets of a karstified Devonian limestone and a fractured Devonian limestone were captured using a ProCon X-ray system equipped with a multifocal X-ray tube, operated at 150 kV and, 140 µA with an exposure time of 160 ms (for more details, see Nehler, 2017; Schepp et al., 2020). The software Avizo from Thermo Fischer Scientific was utilised for pore space mapping, presenting connected pore spaces and assessing the effective pore space. The resolution of the CT scanner was a limiting factor in the effective pore space analysis, given that the scanning resolution is determined by the positioning of the sample between the X-ray tube and detector. Consequently, the dimensions of the sample determine the resolution. The geometrical magnification of the µCT system is determined by the ratio of the source-detector distance to the source-object distance (Voland et al., 2010). All samples were scanned under uniform settings, resulting in voxel sizes of 29 µm.).

Ultrasonic P- and S-wave velocities ($\nu_{P,dry}$, $\nu_{S,dry}$, $\nu_{P,sat}$) were measured for nine sample plugs. The propagation of S-waves in liquids is governed by the medium's viscosity and shear modulus. Since water possesses a shear modulus close to zero, it exerts a negligible influence on S-wave velocities in saturated rock samples, resulting in $\nu_{S,dry} \approx \nu_{S,sat}$. Consequently, S-wave velocity measurements were not performed on water-saturated samples; only P-wave velocities were assessed under these conditions. The ultrasonic transmission setup consisted of a PicoScope 5000 digital storage oscilloscope, an NDT/Epoch 650 waveform generator, and a pair of P- and S-wave transducers from Olympus with a centre frequency of 1 MHz and a sensor diameter of 0.25 in. The waveform generator produced a rectangular pulse with a central frequency of 1 MHz and an amplitude of 400 V, which was applied to the respective P- or S-wave transducer to excite the ultrasonic waves. The transducer pairs were applied to the planar ends of the cylindrical samples with an additional contact pressure of 0.1 MPa, ensuring uniform measurements and appropriate signal quality. The transmitted waveforms were recorded with a sampling interval of 8 ns. For each sample, 500 full waveforms were stacked to obtain an averaged signal, yielding a robust determination of the first arrival traveltime of the transmitted wave. In the case of P-wave measurements, the averaged absolute noise level was approximately 0.16 mV (standard deviation: ±0.08 mV), with a peak amplitude at the first arrival of about 2.5 mV, resulting in a signal-to-noise ratio ranging from 15 to 50 across all nine samples. Correspondingly, for S-wave measurements, the averaged absolute noise level was about 0.05 mV (standard deviation: ±0.02 mV), with a peak amplitude at the first arrival of about 1.1 mV, resulting in a signal-to-noise ratio ranging from 23 to 40. The specific ultrasonic wave velocity ($\nu_{P,S}$) was calculated by dividing the length of each sample (l) by the difference between the wave travel time ($t_{P,S}$) and the system dead time ($t_{sys(P,S)}$). Here, $t_{P,S}$ denotes the first arrival time taken by the ultrasonic wave to traverse through the sample and the system, and $t_{sys(P,S)}$ represents the inherent transmission time through the measurement system (i.e., cables, sensors, etc.). The specific ultrasonic wave velocity was calculated according to

$$\nu_{P,S} = \frac{l}{t_{P,S} - t_{sys}}. \quad (3)$$

The thermal properties of rock samples were assessed using the optical thermal conductivity scanning (TCS) method as outlined by Popov et al. (1999), a widely adopted standard for such analyses (ISRM suggested method; Popov et al., 2016). The TCS system utilised was the model number 2010–013 from Lippmann and Rauen GbR. A stripe of black acrylic paint was applied along the longitudinal axis of each cylindrical sample to ensure uniform heat absorption, as the coating is required to minimise the influence of varying optical reflection coefficients (Popov et al., 1999). The TCS employed infrared sensors to calculate the temperature differential between each sample and a calibrated standard, facilitating the determination of thermal conductivity (λ_{dry}, λ_{sat}) with an accuracy of ±3 %, and thermal diffusivity (α_{dry}, α_{sat}) with an accuracy of ±5 %. Standards with known thermal properties were selected to align with sample ranges, thereby enhancing measurement precision closely. Measurements were conducted on both dry

and water-saturated samples to capture a comprehensive understanding of the thermal properties. This approach was employed immediately after water saturation to minimise moisture loss, and the data were processed using the TCS software. Specific heat capacity (c_{dry}, c_{sat}) was computed from the measured thermal conductivity and diffusivity using the following relation:

$$c_{dry,sat} = \frac{\lambda_{dry,sat}}{\rho_{dry,sat} \cdot \alpha_{dry,sat}}. \quad (4)$$

To estimate the permeability range of the carbonate samples, initial analysis was conducted using standard Darcy flow-through experiments under ambient confinement pressure and temperature. This method offers a minimally invasive approach to evaluating permeability, even in samples exhibiting significant porosity and karst features. The saturated samples were tightly connected using rubber tubing to adapters at both ends. A vertical pipe with a 3 m water column was attached to the upper adapter, thus applying an additional hydrostatic pressure of about 0.3 bar to the sample (Δp). This pressure facilitated gravity-driven axial fluid flow through the sample. The water that percolated through the sample was measured and used to derive the volumetric flow rate (Q). Permeability (k) was calculated using Darcy's law (Darcy, 1856):

$$k = \frac{\eta \cdot Q \cdot l}{A \cdot \Delta p}, \quad (5)$$

where η denotes the dynamic viscosity of water and A is the cross-sectional area of the sample.

3.2.2. Elevated stress and temperature

To assess the permeability of carbonate samples under conditions beyond standard ambient settings (0.1 MPa, 20 °C) and the simplified Darcy flow scenario (0.3 MPa, 20 °C), hydraulic measurements were conducted using a Hoek cell by Control Group, applying triaxial pressure to the core samples. Standardised flow-through experiments were employed to determine permeability (Hoek and Franklin, 1968). Confining pressures of 3.5, 4, 6, 8, and 10 MPa were applied, with the axial pressure consistently maintained at 0.1 MPa above the confining pressure to prevent leakage and flow paths along the piston interfaces that directly contact the sample. The confining pressure was generated using a hand pump and hydraulic oil as the confining medium. Lower pressures were deemed suitable for karstified samples, whereas higher pressures were utilised for denser limestone and dolomite. Each sample was encased in a rubber sleeve and capped with permeable lids. To prevent damage to these sleeves, karstified samples were further protected with an additional rubber tube. A Teledyne ISCO pump system was connected to the lower axial permeability cap of the Hoek cell to facilitate the flow of deionised water through the samples, while the upper axial cap maintained a constant outflow at atmospheric pressure (0.1 MPa). Flow through the samples was induced by maintaining a constant upstream pressure of 2 MPa for confining pressures of 3.5, 4, and 6 MPa, and 8 MPa for a confining pressure of 10 MPa, respectively. Measurements for highly permeable fractured samples were conducted under constant flow conditions due to the significant permeability. Permeability was calculated using Darcy's law, in line with the formulation applied in previous gravity-driven Darcy flow experiments, as detailed in Eq. (6). The primary differences included the use of pressure and temperature-dependent dynamic viscosity as described by Wagner (2009), and the monitoring of volumetric flow using the Isco Pump Control software during each test.

To effectively characterise reservoir properties in a laboratory setting, it is essential to simulate in-situ conditions that encompass elevated pressures and temperatures. These simulations enable a comprehensive evaluation of hydraulic properties, including permeability, specific storage capacity, hydraulic diffusivity, and volumetric deformation. The study focused on selected representative samples of dolostone and karstified limestone, which are considered the most promising for enhanced reservoir performance. A thermo-triaxial deformation apparatus was employed to apply conditions corresponding to depths between 200 and 3,000 m (5 to 75 MPa and 25 °C to 100 °C). The oscillatory pore-pressure method was utilised to derive the full set of hydraulic properties (Kranz et al., 1990; Fischer, 1992). Saturated samples, encased in Viton® tubing and fitted with a circumferential extensometer, were positioned between axial pistons within the pressure vessel (Sepúlveda et al., 2020). These pistons, designed with internal bores, maintained a constant fluid pressure connected to independent pore-fluid systems (upstream and downstream) with dedicated pressure transducers. Hydraulic oil and distilled water were used for confining and pore-fluid systems, respectively. Servo-hydraulic pressure intensifiers modulated confining pressure, upstream pore-fluid pressure, and axial piston movement. The pressure vessel, enveloped by a heating jacket and equipped with a thermocouple through a high-pressure-high-temperature feedthrough, ensured precise temperature control and thermal equilibrium following a 12-hour equilibration period at 100 °C.

Hydrostatic experiments were carried out under nominally drained conditions with a constant pore pressure of 30 MPa. Confining pressures were incrementally increased from 5 MPa to 75 MPa, then adjusted to 35 MPa, while the samples were heated to 100 °C to assess the thermal effects. Total porosity ($\Delta\phi_{tot}$) was evaluated by subtracting axial (ε_{ax}) and radial strain data (ε_{rad}) recorded by axial displacement transducers and the circumferential extensometer, respectively, from the initial total porosity as determined at ambient conditions:

$$\phi_{tot} = \phi_{tot} - (\varepsilon_{ax} + 2\varepsilon_{rad}) \quad (6)$$

Using the same principle, the density of the sample under elevated stress conditions was calculated by adjusting the density measured under ambient conditions to account for the changes in total porosity.

Critical crack-closure pressures, which mark transitions from linear to nonlinear petrophysical behaviour, were identified through porosity-pressure logs (Walsh, 1965; Mavko and Nur, 1978). The oscillatory pore-pressure method involved continuous oscillation with an amplitude of 1 MPa and a period of 400 s. Pressure data were detrended to remove transients and underwent Fourier analysis over ten oscillation periods to calculate averaged amplitude ratios and phase shifts between upstream and downstream pressure (for details see Ahrens et al., 2018). These values were used to derive permeability (k) and specific storage capacity (s) (Bernabé et al., 2006). Hydraulic diffusivity (D_{hyd}) was calculated using the pressure- and temperature-dependent viscosity according to Wagner (2009), using the equation

$$D_{hyd} = \frac{k}{\eta \cdot s}. \quad (7)$$

3.3. Geothermal heat-in-place estimation

The geothermal potential of the Middle Devonian limestones was evaluated using the volumetric-deterministic approach proposed by Muffler and Cataldi (1978). This method estimates the thermal energy stored, referred to as Heat-In-Place (HIP), within a refined reservoir volume composed of rock and pore fluid. It assumes homogeneous density and specific heat capacity, as well as a defined temperature differential relative to a reference base temperature (Marrero-Diaz et al., 2015).

In this study, key petrophysical parameters were derived from laboratory measurements, including effective porosity and bulk density of the Devonian carbonates. To capture the full variability of the dataset, minimum and maximum values were utilised irrespective of facies classification. The highest porosity values (up to 14.24 %) were associated with karstified limestones, whereas the lowest porosities (down to 0.62 %) were measured in the least-altered micritic carbonates. For the Monte Carlo simulations of the consolidated reservoir, the maximum measured dolostone porosity of 4.65 % was used, while the corre-

sponding micritic or compact carbonate samples represented the lower porosity values. Similarly, density values were inversely correlated with porosity, with the densest samples corresponding to compact, unaltered limestone and the lowest densities occurring in highly karstified intervals. Given the pronounced variability in the petrophysical dataset, a Monte Carlo simulation was employed to model parameter distributions assuming a normal distribution. Based on this statistical framework, the bulk volumetric heat capacity (c) was calculated following the formulation of Limberger et al. (2018) and Marrero-Diaz et al. (2015):

$$c = \phi_{\mathrm{eff,MC}} \cdot \rho_{\mathrm{wt}} \cdot c_{\mathrm{wt}} + \left(1 - \phi_{\mathrm{eff,MC}}\right) \cdot \rho_{\mathrm{s,MC}} \cdot c_{\mathrm{s,MC}}. \quad (8)$$

Here, $\phi_{\mathrm{eff,MC}}$, $\rho_{\mathrm{s,MC}}$ and $c_{\mathrm{s,MC}}$ represent the effective porosity, bulk density and specific heat capacity of the carbonate rocks, respectively, as estimated through the Monte Carlo simulation. Reservoir thickness estimates were based on regional stratigraphic models provided by the Geological Survey of North Rhine-Westphalia (Geologischer Dienst NRW, 2023) and supplemented by values from Krebs (1974). Subsurface temperature estimates were derived from regional thermal gradient data, applying an average geothermal gradient of 30 °C/km, calibrated against the temperature-depth model of GD NRW (Fig 2). The total Heat-In-Place (H) was calculated using the following equation (Limberger et al., 2018):

$$H = c \cdot (T - T_0) \cdot h, \quad (9)$$

where T refers to the mean reservoir temperature (i.e., the sum of the modelled subsurface temperature and the mean annual surface temperature of 10 °C), T_0 is the base surface temperature, and h is the reservoir thickness. The study area is discretised into a raster of 1,339 cells, each representing an area of 62,500 m^2. Heat-in-place estimates were obtained by randomly sampling from the probability distributions of bulk heat capacity and applying the corresponding values to each grid cell. The calculations were implemented using the geothermal assessment framework of Alms et al. (2025), based on 5,000 Monte Carlo iterations. From the resulting cumulative probability distribution, estimates of proven (*P90*), probable (*P50*), and possible (*P10*) heat resources were extracted for a potentially karstified reservoir and a consolidated reservoir. All input parameters used are summarised in Table 1.

Table 1
Output and input parameters with associated symbols, units and fixed values.

Output parameter	Input parameter	Symbol	Unit	Value
	Surface temperature	T_0	K	283.15
	Aquifer thickness	h	m	330 … 860
	Reservoir temperature	T	K	283.15 … 377.15
	Aquifer bulk heat capacity	c	J m^{-3} K^{-1}	
	Porosity (karstified)	φ	-	0.62 … 14.24
	Heat capacity water	c_w	J kg^{-1} K^{-1}	4190
	Heat capacity rock (karstified)	c_r	J kg^{-1} K^{-1}	800 … 1,060
	Density water	ρ_w	kg m^{-3}	997
	Density reservoir rock (karstified)	ρ_r	kg m^{-3}	2,284 … 2,697
	Devonian carbonate area in Iserlohn	A	m^2	83,736,734
	Raster area in Iserlohn	A_r	m^2	62,500
Heat-in-place karstified		H	TJ m^{-2}	87 … 110
	Porosity (consolidated)	φ	-	0.62 … 4.65
	Heat capacity rock (consolidated)	c_r	J kg^{-1} K^{-1}	807 … 892
	Density reservoir rock (consolidated)	ρ_r	kg m^{-3}	2,653… 2,697
Heat-in-place consolidated		H	TJ m^{-2}	89 … 97

4. Results

4.1. Facies, petrography and macroscopic meteoric karst features

4.1.1. Macroscopic drill core description

The three drill cores (BK-6, BK-9 and BK-11) studied were described from top to base with respect to (1) depositional facies, (2) fossil

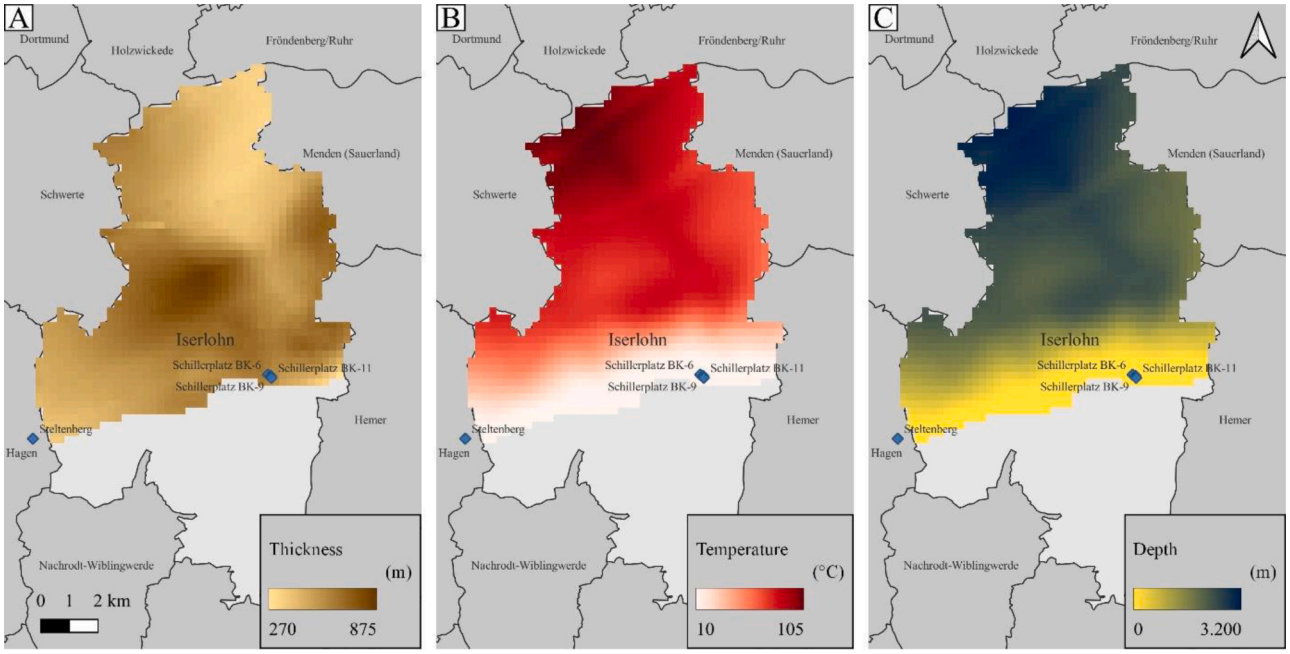

Fig. 2. Input parameters in grid format. Each cell equals an area of 250 × 250 m. (**A**) shows the thickness of the Devonian carbonates, (**B**) indicates the temperature distribution correlating with burial depth and (**C**) displays the top of the Devonian carbonates. The geographical location of the Steltenberg quarry and the three boreholes at Schillerplatz in Iserlohn is indicated by blue diamonds. The samples for the study were obtained from boreholes Bk-6, Bk-9, and Bk-11.

assemblage, (3) macro-porosity, and (4) macroscopic evidence of meteoric karst features. Core lengths are 48 m for BK-9, 28 m for BK-9, and 15 m for BK-11 (Fig 3). The carbonate rock colours range from grey to creamy to reddish-brown. Grey hues indicate reducing conditions and are typical of least-altered limestones (Fig 4), while creamy to brownish tones are characteristic of dolomitised intervals and often associated with ferroan dolomite and oxidising diagenetic conditions (Flügel, 2010). Strongly leached sections appear yellowish to brownish.

(1) Following Pederson et al. (2021), a petrographic classification scheme was applied to differentiate carbonate lithologies based on

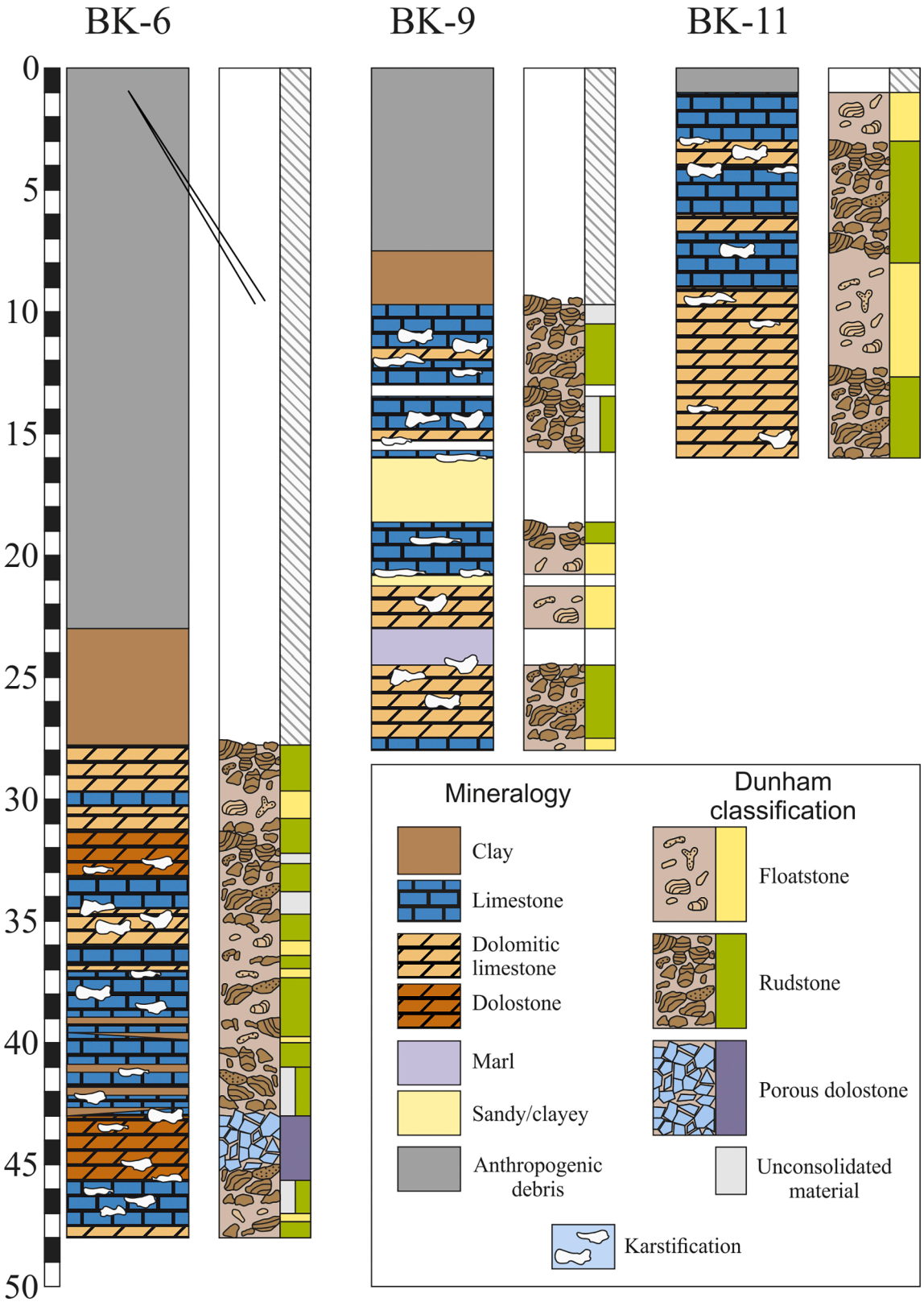

Fig. 3. Drill core sketch of Core BK-6, BK-9 and BK-11 with sedimentological characteristics.

Fig. 4. Drill core section of core BK-6 at a depth of 43–48 m. Red X indicates a sample point in the karstified area of the core.

dolomite content, distinguishing limestone (<20 % dolomite), dolomitic limestone (20–75 % dolomite) and dolostone (>75 % dolomite). Nine representative subsamples were collected for further analysis. XRD and thin section analysis were conducted on all samples. Of these, seven were classified as limestone and two as dolostone. Three of the limestone samples exhibit pervasive karstification due to meteoric conditions.

(2) The uppermost sections of all three cores consist of unconsolidated material, including clay, sand, and anthropogenic debris (Fig 3). The transition of the surficial regolith to Devonian limestone and dolomitic limestone, is a hiatal interval of approximately 370 Myr, situated about 27.8 m below the land surface (core top) in the case of BK-6, 10.5 m below the land surface for BK-9 and 2.2 m below the surface for drill core BK-11. The carbonate depositional facies alternate between floatstones and rudstones (Dunham, 1962; Embry and Klovan, 1971), with *Amphipora* stromatoporoids as the primary fossil components in a wackestone matrix. General descriptions of the facies along the drill cores are illustrated in Fig 3. BK-6 cored 20.2 m of carbonate, BK-9 cored 17.5 m of carbonate, and BK-11 cored 13.8 m of carbonate rock. All core logging results and facies distribution are summarised in Fig 3.

BK-6 comprises 20.2 m of carbonate rock, of which 74 % is rudstone, 12 % floatstone, and 14 % porous dolostone. BK-9 contains 17.5 m of carbonate, consisting of 58 % rudstone and 23 % floatstone. BK-11 comprises 13.8 m of carbonate, with 58 % rudstone and 42 % floatstone. In terms of carbonate type, BK-6 is composed of 50 % limestone, 26 % dolomitic limestone, and 24 % dolostone. BK-9 consists of 45 % limestone, 31 % dolomitic limestone, and 24 % intervals of sandy to marly sediments. BK-11 comprises approximately 45 % limestone and 55 % dolomitic limestone.

(3) Intervals of core loss were documented in BK-9 between 13.0 and 13.5 m, and between 15.4 and 15.6 m. Sandy to clayey layers occur from 16.0 to 18.5 m and again from 20.8 to 21.2 m, while a marly interval is present between 23.0 and 24.5 m. In BK-6, dolostone was identified in a section ranging from 30.1 to 33.0 m, and highly porous dolostone occurs in the interval from 43.0 to 45.5 m.

(4) Macroscopic evidence of meteoric karstification, defined as dissolution features driven by rainwater and soil-derived CO_2 (cf. Bosak et al., 1989), is present at the interface between unconsolidated cover and Devonian carbonate bedrock, and extends downward into the underlying strata. Karst features occur as irregular to elongate cavities up to several centimetres in diameter, often exhibiting brown staining and clay infill (Fig 4). These features are most common in dolomitic or partially dolomitised carbonates (Fig 4). Karstification typically produces rounded dissolution cavities, particularly near the contact with overburden. It frequently exceeds the physical limits of the recovered core. In the lower part of core BK-6 (43.7 to 45.8 m), porous dolostone with abundant karstified intervals was observed. Here, smaller dissolution features (several centimetres in size) frequently show matrix leaching in the vicinity of fossil fragments, forming interparticle porosity. This phenomenon is especially pronounced in intervals rich in *Amphipora stromatoporoids*.

4.1.2. *Transmitted light petrography and paragenetic phases*

Of the 26 thin sections analysed, 10 derive from comparably well-preserved Devonian limestone, seven from dolostone, and nine from karstified limestone. The cement phase nomenclature follows Mueller et al. (2024). Based on transmitted light and cathodoluminescence microscopy, the following paragenetic succession, from oldest to youngest, was identified:

The least-altered limestone contains abundant *Amphipora stromatoporoids* and tabulate coral embedded in a fine-grained (wackestone) matrix, forming the substratum for all subsequent cement generations (Fig 5A; MK matrix). These samples exhibit an orange to red luminescence, indicative of partial replacement of the original carbonate (Fig 5B). Veins and drusy pores are commonly filled with a paragenetic succession of marine to burial carbonate fabrics. The earliest marine cement phase comprises radiaxial fibrous calcite (RFC) and dog-tooth spar (DT), forming fringes up to 500 μm thick and displaying dark red-violet, zoned luminescence (Fig 5C, D).

Three generations of dolomite cements were identified, alongside various hydrothermal and meteoric phases that partially to completely replaced the original matrix. The earliest dolomite phase (Dol 1) is characterised by medium-crystalline (ca. 0.4 mm), planar-s dolomite with patchy dark red luminescence (Figs. 5A, B). Next, blocky calcite cement (low-Mg calcite - LMC 1) fills larger pores and displays strongly zoned crystals alternating between bright and dull red luminescence (Figs. 5C, D). The second dolomite generation consists of two components: brownish, fine-to medium-crystalline matrix dolomite (Dol 2A; planar-s to non-planar) and greenish to brownish saddle dolomite (Dol 2B) with sweeping extinction and red-orange luminescence (Fig 5E, F; cf. Zhang et al., 2025). Partial dedolomitisation of this phase (Dedol 1) resulted in dolomite morphologies with orange-red luminescence (Fig 5E, F). Both dolomite types are often overgrown by a second generation

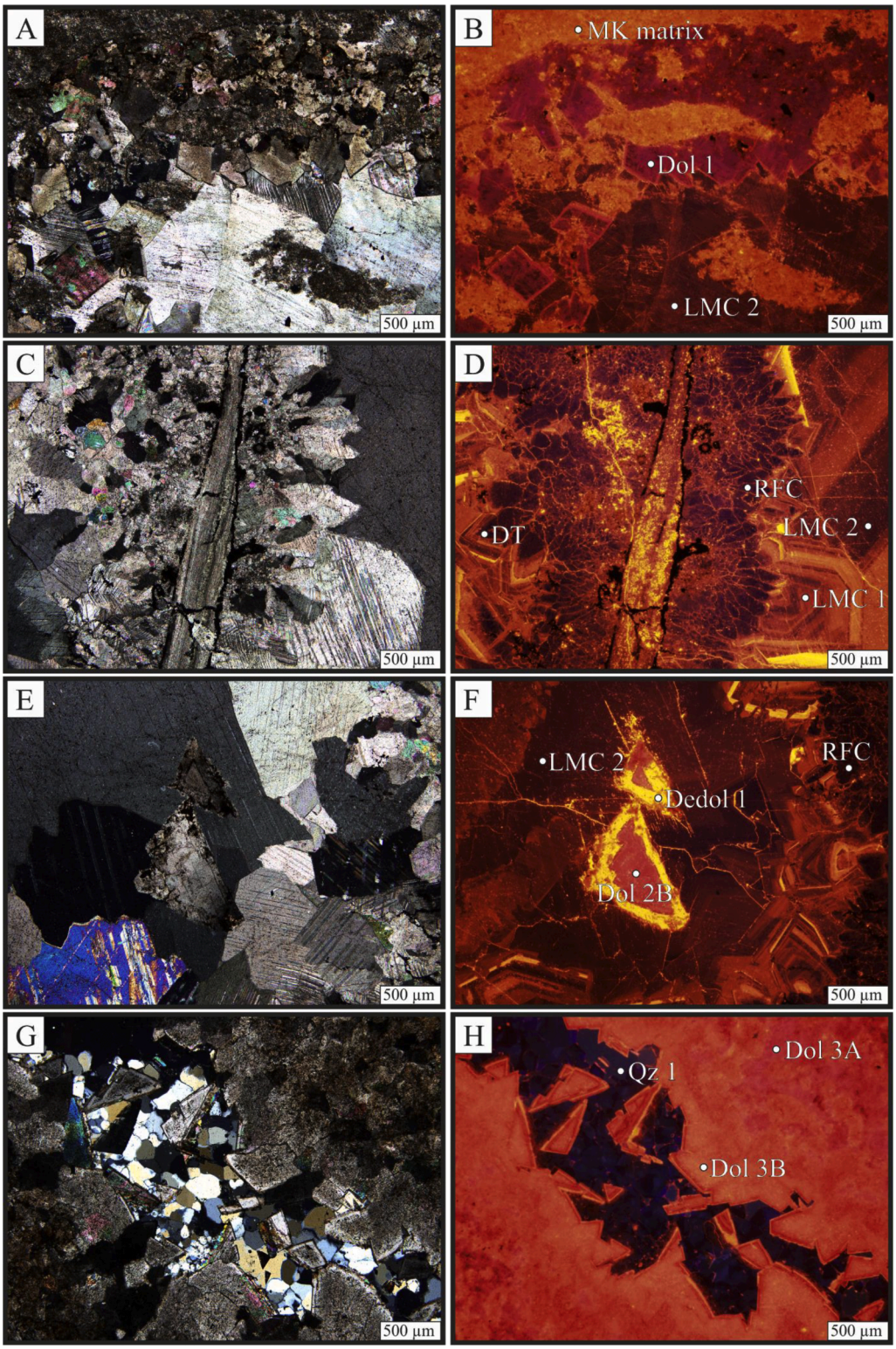

Fig. 5. Cross-polarised light (left) and corresponding cathodoluminescence image (right) of the carbonates at the Schillerplatz in Iserlohn. (**A, B**) Limestone with dolomite phase 1 and blocky calcites (LMC 1). (**C, D**) Radiaxial fibrous cements, dog teeth and blocky calcite cements (1 & 2) as infilled in a cavity inside a fossil. (**E, F**) Pore filled with RFC and blocky calcite, as well as Dol 2B saddle dolomite with a Dedol 1 rim. (**G, H**) Post-Variscian dolomites (Dol 3) and quartz precipitation.

of blocky calcite (LMC 2), which exhibits weakly zoned, dull red luminescence (Fig 5C, D).

The third, paragenetically youngest dolomite generation (Dol 3) occurs as medium- to coarse-crystalline (0.2–0.6 mm) planar-s dolomite (Dol 3A) with red luminescence, and as coarse saddle dolomite (Dol 3B), which exhibits orange to red luminescence and sweeping extinction under crossed polarised light (Figs. 5E, F). This phase was locally dedolomitised (Dedol 2), preserving crystal outlines but exhibiting patchy yellow luminescence (Fig 6A, , E, F). In vuggy porosity, Dol 3 and Dedol 2 are commonly overgrown by fine- to coarse-grained quartz (Qz 1 and Qz 2, approximately 0.4 mm), which exhibit dark blue and yellowish luminescence (Fig 6C, D). These, in turn, are occasionally

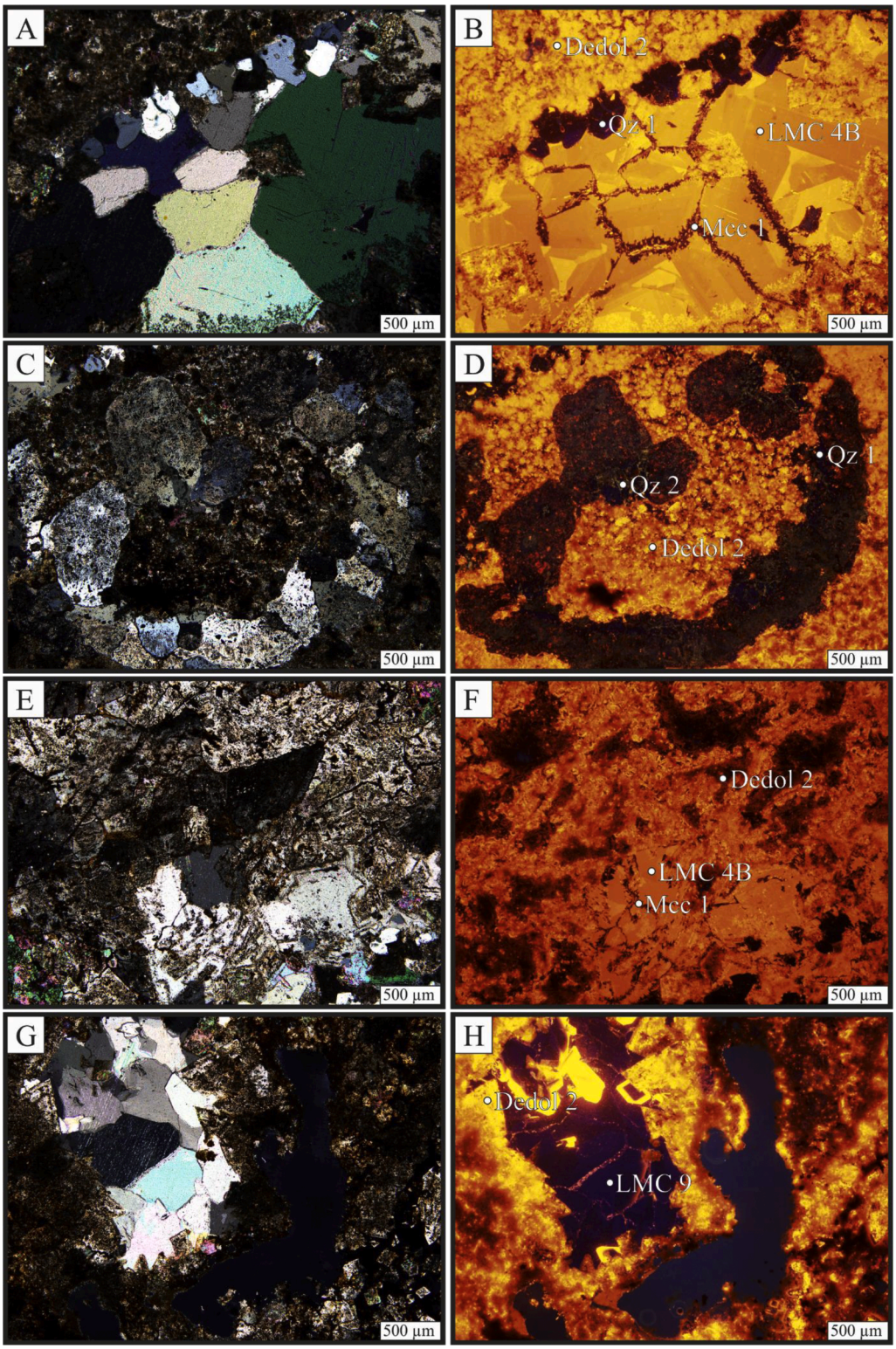

Fig. 6. Cross-polarised light and corresponding cathodoluminescence image of the carbonates at the Schillerplatz in Iserlohn. (**A, B**) Hydrothermal calcite cements and quartz precipitation with typical features of later overprinting by meteoric calcites precipitating along grain boundaries. (**C, D**) Quartz in dedolomitised matrix. (**E, F**) Dedolomitised saddle dolomites, hydrothermal calcites and meteoric calcites precipitating along grain boundaries. (**G, H**) Late meteoric calcite cement, characterised by blocky calcite as a void-filling mineral. Leaching effects caused rounded voids in the matrix.

overgrown by macrocrystalline blocky calcite with yellowish luminescence (Fig 6E, F; LMC 4B). Late fissure-filling meteoric calcite cements (Mcc 1) exhibit no luminescence. The final paragenetic phase consists of macrocrystalline (0.4–0.6 mm) blocky calcite (LMC 9) with dark blue luminescence, often associated with late-stage leaching and karstification (Fig 6G, H).

4.2. Petrophysical characteristics

4.2.1. Bulk, acoustic and thermal properties at ambient conditions

The petrophysical dataset obtained from laboratory analysis reveals significant differences between karstified and non-karstified carbonates in terms of bulk properties and physical variability (Fig 7; Table 1). Among all lithotypes, karstified limestone samples exhibit the largest internal variability, as indicated by the broadest range in measured porosity, density, thermal and acoustic parameters. In contrast, dolostone and relatively unaltered limestone samples show comparatively narrow data ranges. When accounting for analytical uncertainties, bulk density and ultrasonic wave velocities do not allow for a clear distinction between limestone and dolostone. Transport-related properties, including ultrasonic wave velocity and thermal conductivity, exhibit a positive correlation with bulk density (Fig 7B, C). Specific heat capacity does not exhibit a systematic correlation with porosity; values across all lithologies lie within a narrow and overlapping range.

Bulk petrophysical properties differ systematically between lithological groups. Grain densities vary across lithologies, with mean values of ~2,725 kg/m^3 for limestone and karstified limestone, and slightly higher values of ~2,810 kg/m^3 for dolostone. The mean bulk densities of limestone and dolostone samples are both ~2,575 kg/m^3. The range of values overlaps, and the two lithologies cannot be reliably distinguished based solely on bulk density. In contrast, karstified limestone samples exhibit lower mean bulk densities of ~2300 kg/m^3. Effective and total porosity values of limestone and dolostone are also comparable, with average values of ~1.5 % (effective) and 4.6 % (total). Karstified limestones yield markedly higher mean values, with ~12 % effective and ~14.5 % total porosity. On average, this difference amounts to ~2.6 %, corresponding to ~18 % of the total porosity, and represents unconnected pore volume.

Elastic wave velocities and thermal properties provide further differentiation among the studied lithologies (Fig. 7C, D). While dolostone and limestone samples yield comparable values, karstified carbonates consistently exhibit reduced elastic and thermal properties (Fig 7B, C, E). Under dry conditions, limestone and dolostone samples record the highest P-wave velocities, averaging ~6,000 m/s and ~5,800 m/s, respectively. Shear wave velocities follow a similar trend, with mean values of ~3,400 m/s for limestone and ~3,200 m/s for dolostone. The ranges of both parameters largely overlap, and no distinction can be made between these two lithologies based solely on acoustic velocities. In contrast, karstified limestone samples exhibit lower velocities, with average P-wave and S-wave velocities of ~5000 m/s and ~2,850 m/s, respectively. Dry thermal conductivity values follow a similar lithological pattern, averaging ~3.3 W/m·K in limestone, ~3.0 W/m·K in dolostone, and ~2.9 W/m·K in karstified limestone. Specific heat capacities range from 800 to 900 J/kg·K, with karstified samples tending toward the upper end of this spectrum. Given the high analytical uncertainty (up to 50 %), no systematic lithological trend can be confirmed. Average thermal diffusivities are ~1.3 × 10^{-6} m^2/s (limestone), ~1.4 × 10^{-6} m^2/s (dolostone), and ~1.1 × 10^{-6} m^2/s (karstified limestone). Upon water saturation, P-wave velocities and thermal parameters increase across all lithologies. Relative increases of ~5 % (limestone), ~10 % (dolostone), and ~7 % (karstified limestone) were observed in P-wave velocity. The most pronounced relative change is observed in the specific heat capacity of karstified carbonates, which increases by ~40 %. Thermal conductivity increases by ~25 % on average in all samples.

4.2.2. Hydraulic properties at reservoir conditions

Hydraulic properties were determined using a combination of laboratory test setups adapted to the specific lithological characteristics and expected permeability ranges. For limestone and dolostone samples, permeability was measured using a Hoeck-cell apparatus and a thermal triaxial cell (Fig. 7F; Figs. 8C, E, G). In contrast, the predominantly secondary permeability in karstified samples was assessed using a low-pressure flow-through system based on Darcy's work (Darcy, 1856) (Fig. 7F). Across all setups, the obtained results are consistent and methodologically comparable. Measured permeabilities span several orders of magnitude depending on lithology. Karstified limestone samples exhibit the widest range, with values between ~5 × 10^{-17} and 1 × 10^{-15} m^2 (Fig 7F and Fig 8D). Dolostone samples yield permeability values between ~1 × 10^{-19} and 1 × 10^{-17} m^2. In contrast, unaltered limestone samples show the lowest permeabilities, ranging from ~1 × 10^{-19} to 3 × 10^{-18} m^2 (Fig. 7F). Fractured limestone samples tested at laboratory scale exhibit permeabilities of up to 1 × 10^{-14} m^2.

Under elevated effective pressures of up to 110 MPa (equivalent to depths of ~3 km), dolostone samples exhibit a slight decrease in permeability. A distinct initial reduction in permeability is observed up to ~50 MPa, beyond which the pressure–permeability relationship transitions into a linear regime. This threshold is indicated by the grey vertical bar in Fig 8. Overall, dolostone permeability decreases by ~half an order of magnitude under maximum tested pressure conditions, reaching values of ~1 × 10^{-19} m^2. The same sample was also used to determine specific storage capacity and hydraulic diffusivity. While storage capacity remained largely pressure-independent (~5 × 10^{-12} Pa^{-1}), hydraulic diffusivity decreased by roughly half an order of magnitude to ~1 × 10^{-3} m^2/s. Karstified limestone exhibits higher hydraulic diffusivity (~5 × 10^{-2} m^2/s) and specific storage capacity (~1 × 10^{-11} Pa^{-1}) under comparable conditions (Fig 8F, H). Additional tests conducted on dolostone under reservoir-relevant temperature conditions (100 °C) reveal that elevated temperature has no discernible influence on pressure sensitivity. However, it reduces permeability and specific storage by approximately one-quarter and one-half of an order of magnitude, respectively, resulting in a net reduction of hydraulic diffusivity by about one order of magnitude. These results suggest a general trend of decreasing hydraulic performance under reservoir conditions. Under identical pressure and temperature conditions, bulk density as well as effective and total porosity were determined. With increasing effective pressure, porosity decreases approximately linearly, while temperature variations exert only a minor influence. The corresponding bulk density values, calculated from the measured porosity data under the assumption of mass conservation, display an inverse trend with respect to porosity.

4.2.3. Pore and karst architecture from μCT imaging

High-resolution X-ray micro-computed tomography (μCT) was applied to one karstified limestone sample and one fractured limestone sample to visualise internal pore structures at the sub-centimetre scale (Fig 9). The scans provide three-dimensional representations of the pore geometries preserved in the analysed specimens.

The karstified limestone sample (ISMK-002) reveals an irregular pore architecture. The largest spherical volumes that fit into the connected pore space reach diameters of ~5 mm (Fig 9A,B). Elongated pores with opening widths of up to ~5 mm and lengths exceeding 10 mm were also identified. Pores larger than ~40 mm were not captured due to the limited dimensions of the scanned specimen. Microporosity below the voxel resolution of ~30 μm could not be resolved.

In contrast, μCT imaging of the fractured limestone sample (ISMK-003) shows a single open fracture extending continuously from the upper to the lower boundary of the specimen (Fig 9C,D). The fracture aperture measures approximately 250 μm. No additional internal voids were resolved at the applied scanning resolution.

4.3. Heat-in-place modelling

The total estimated heat content within the potentially karstified Devonian carbonates in the Iserlohn area ranges from 87 TJ (90th percentile, P90) to 110 TJ (10th percentile, P10). This variability reflects the combined influence of spatial heterogeneity and parameter uncertainty (Table 2). The heat-in-place calculations are presented on a grid with individual cells covering 62,500 m^2. Energy density estimates

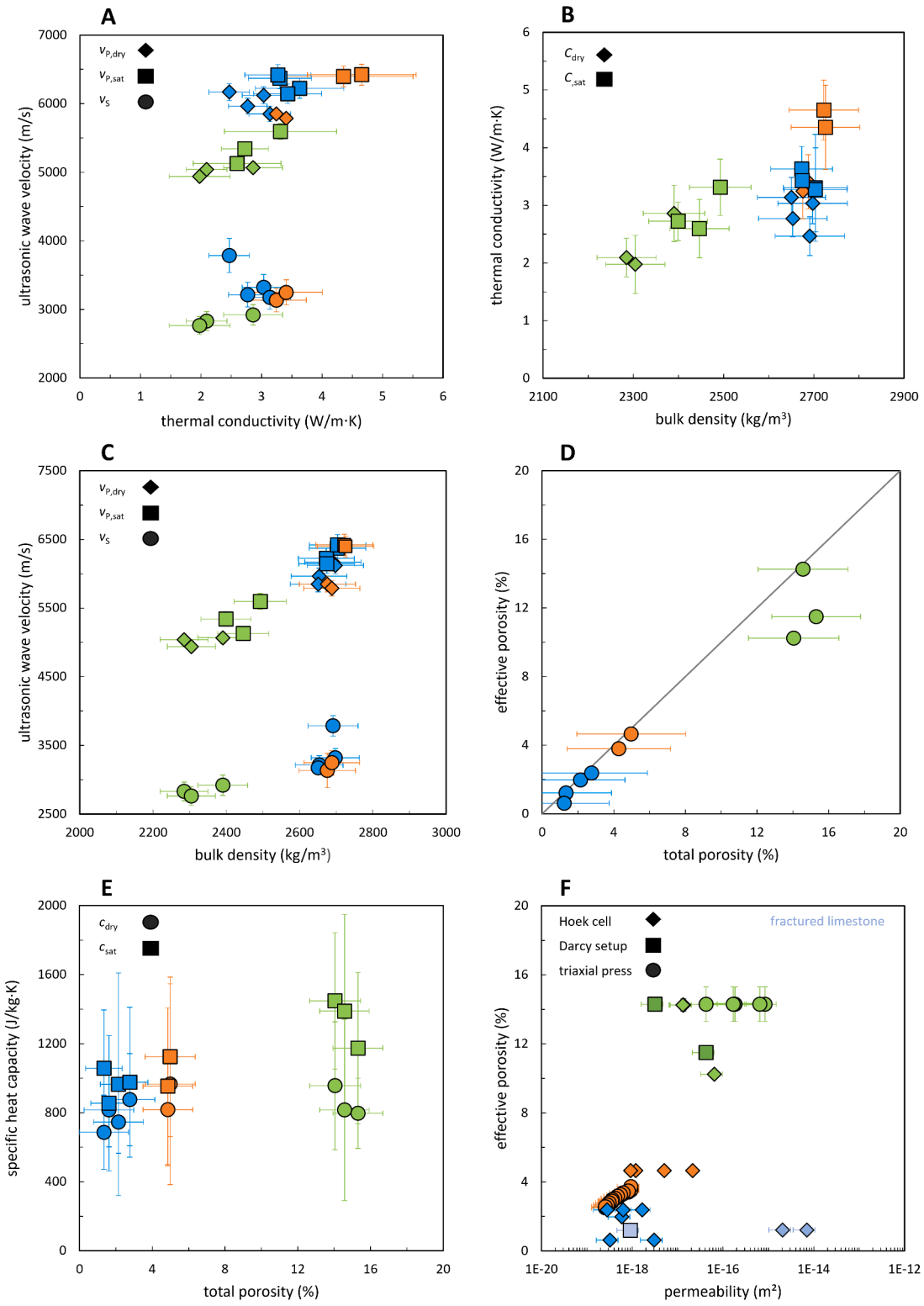

Fig. 7. Mean results of petrophysical measurements under ambient conditions (**A** – **E**) and elevated pressure conditions (**F**). Blue-coloured symbols represent Devonian limestone, orange symbols display dolostones, and green symbols represent karstified limestones. Error bars represent the range of the Gaussian errors by error propagation. (**A**) ultrasonic wave velocities versus thermal conductivity. (**B**) displays thermal conductivity versus bulk density. (**C**) shows ultrasonic wave velocities versus bulk density. (**D**) φ_{tot} versus φ_{eff}, with the line of identity marking the upper limit, since $\varphi_{tot}/\varphi_{eff} \geq 1$. (**E**) specific heat capacity versus φ_{tot}. (**F**) φ_{eff} versus permeability, with measurements conducted under three different methods.

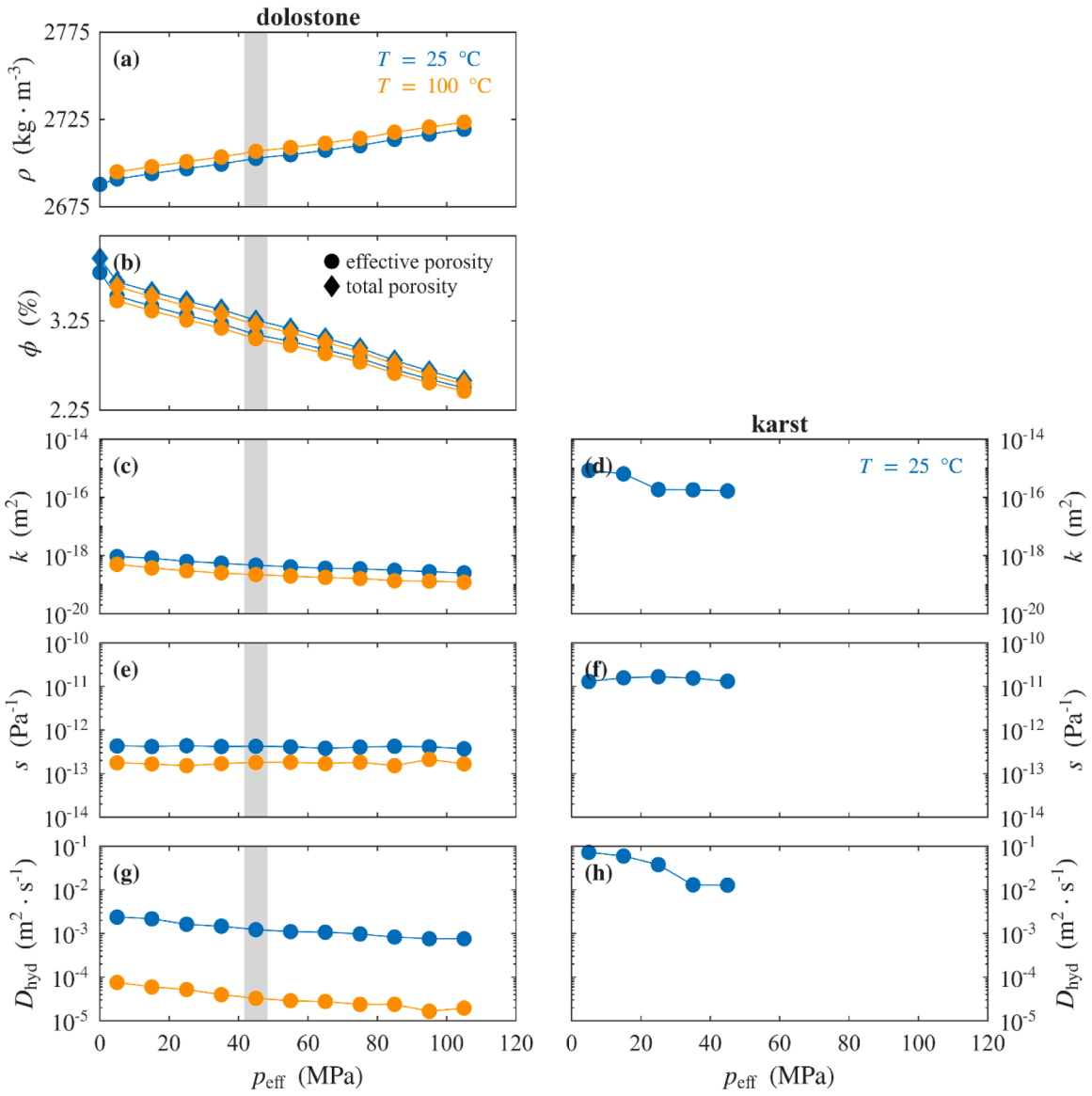

Fig. 8. (**a**) Bulk density ρ, (**b**) porosity ϕ, (**c, d**) permeability k, (**e, f**) specific storage capacity, and (**g, h**) hydraulic diffusivity D_{hyd} as functions of effective pressure, as determined from compaction experiments during hydrostatic pressurisation and depressurisation of carbonate samples. Panels on the left correspond to dolostone, whereas panels on the right depict results for karstified limestone. Marker style and colour indicate the experimental temperature (T), as specified in the legend. Grey vertical bars denote the empirically determined critical crack-closure pressure.

within the Devonian carbonates range from 0 to 160 GJ/m^2. Maximum values reach 129 GJ/m^2 at the P90 percentile and 163 GJ/m^2 at the P10 percentile (Fig 10). High heat-in-place values are concentrated centrally within the Devonian carbonate distribution and in the north-western sector of the study area. The zone of maximum heat-in-place in Iserlohn exhibits an elliptical shape, with its major axis oriented southwest to northeast. Heat content generally decreases toward the southern part of the area and increases toward the northwest, with an anomalous lower-energy zone observed northeast of the main distribution. At the Schillerplatz drill core site, the estimated heat content is zero for all percentiles. Note that the values shown are static and do not account for potential dynamic effects, such as fluid-rock interaction, fluid migration, or karstification. In comparison, the heat-in-place for a consolidated carbonate reservoir ranges from 89 to 97 TJ, representing the 90th percentile (P90) to the 10th percentile (P10). At the P90 percentile, the consolidated scenario exceeds the karstified scenario by 2.3 TJ; at the P50 percentile, it is 5 TJ lower; and at the P10 percentile, the karstified scenario exceeds the consolidated by 13 TJ.

5. Discussion

5.1. Depositional environment and facies architecture

Despite detailed previous work based on outcrop data and their correlation (Krebs, 1974; Pederson et al., 2021; Lippert et al., 2022; Mueller et al., 2024), the spatially and stratigraphically complex Devonian carbonate system in the subsurface of NRW remains insufficiently understood. The primary reason is that, for over a century, research focus has been predominantly on the coal-bearing Carboniferous units. Moreover, currently available data indicate a spatially and temporally complex facies architecture of the Devonian strata, which is overprinted by regional fault zones and a complex diagenetic history (Fig 11). The authors emphasise that this complex diagenetic history is often directly linked to the depositional and tectono-diagenetic setting and the specific rock properties at a given study site. Drill cores from Iserlohn cover middle Devonian reefal units, primarily consisting of reefal material shed from bioherms. The occurrence of grainstones

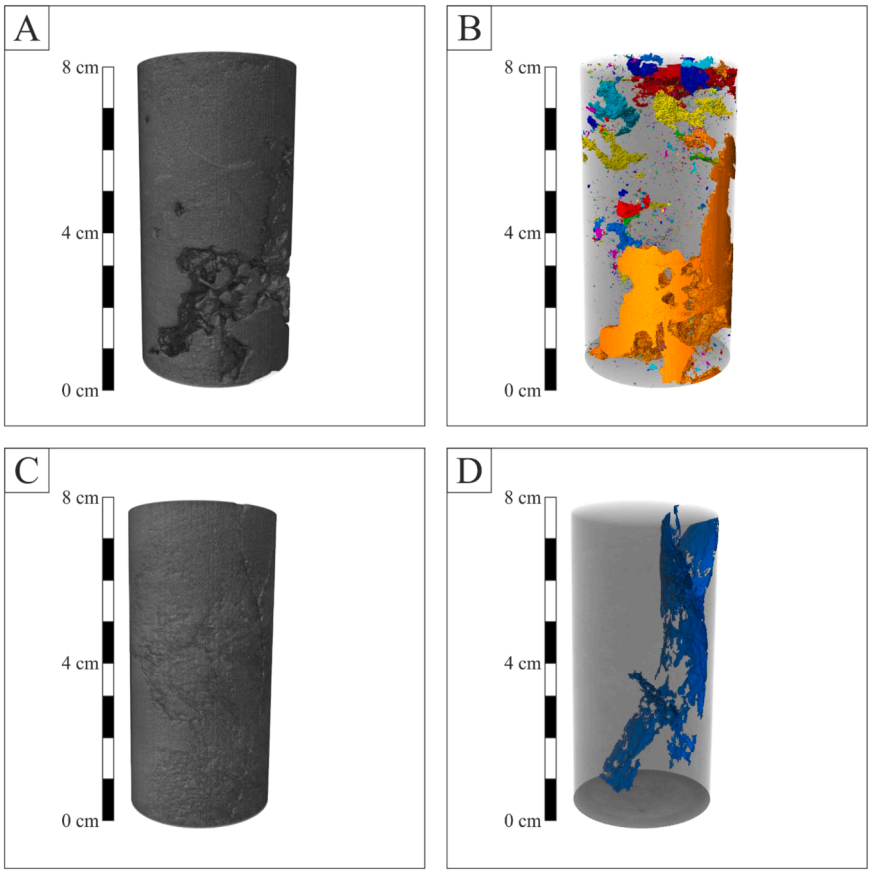

Fig. 9. µCT-scans of a karstified Devonian carbonate (**A, B**) and a scan of a fractured Devonian limestone (**C, D**). The left images are grayscale and show the sample appearance, while the right images display the internal structure of the samples. Same colored clouds show interconnected pores.

indicates a high-energy environment in the wave-exposed zone of a platform (or ramp). Similarly, floatstones are characteristic of shallow marine settings, predominantly lagoonal (refer to Unger et al. (2023) for a recent discussion of Devonian carbonate facies in the region). In particular, the *Amphipora* stromatopore morphology, characterised by finely branched morphotypes (3 to 5 mm in diameter), points to a lagoonal- or back-reef environment, either characterised by a low wave and current energy or a habitat below the average wave base (Garland et al., 1996; Löw et al., 2022). The non-carbonate units overlying the carbonate strata represent anthropogenic deposits filling former galmei mines ($ZnCO_3$; zinc carbonate) at Schillerplatz (Fig 3) (Clostermann, 2018) and were not further considered.

5.2. Paragenetic succession

The succession of diagenetic events that have affected the limestone at the Schillerplatz drill site is documented and discussed here from the perspective of rock properties. Cement precipitation in pore spaces reduces porosity, whereas dissolution processes create secondary porosity (see Mueller et al., 2024) and references therein for a summary of diagenesis of Devonian carbonate units). All cement fabrics discussed below are illustrated in the paragenetic sequence shown in Fig 12.

The paragenetic succession of Devonian carbonates at Schillerplatz comprises bulk limestones (rudstones to floatstones) overprinted by marine and burial cementation. Radiaxial fibrous and dog tooth cement indicate phreatic-marine to (shallow) marine-burial conditions (Flügel,

Table 2
Mean values and standard deviation of the basic petrophysical properties derived at ambient conditions. Samples include limestones, dolostones and karstified limestones. Permeability measurements of limestones and dolostones were carried out utilising a Hoek cell with elevated stress conditions. Karstified samples were measured using an experimental setup according to Darcy's law under ambient conditions.

Parameters	Limestone	Fractured limestone	Dolostone	Karstified carbonates
Number of samples (-)	3	1	2	3
$v_{P,\ dry}$ (m s)	13.30 ± 0.28	12.97	13.78 ± 0.08	16.03 ± 0.16
$v_{P,\ sat}$ (m s)	12.74 ± 0.21	12.56	12.51 ± 0.02	15.03 ± 0.53
$v_{S,\ dry}$ (m s)	23.85 ± 1.62	22.46	25.10 ± 0.45	28.31 ± 0.65
ρ_{bulk} (kg m^{-3})	2680 ± 0.20	2730	2680 ± 0.10	2330 ± 0.50
ρ_{grain} (kg m^{-3})	2720 ± 0.10	2690	2740 ± 0.40	2730 ± 0.40
φ_{tot} (%)	1.96 ± 0.58	1.34	4.49 ± 0.47	14.64 ± 0.52
φ_{eff} (%)	1.55 ± 0.68	1.22	4.23 ± 0.43	11.99 ± 1.67
λ_{dry} (W m^{-1} K^{-1})	2.40 ± 0.17	2.47	2.81 ± 0.49	2.00 ± 0.30
λ_{sat} (W m^{-1} K^{-1})	2.65 ± 0.14	3.31	3.03 ± 0.62	2.21 ± 0.24
c_{dry} (J kg^{-1} K^{-1})	806.70 ± 41.70	724.34 ± 37.67	891.94 ± 73.93	841.17 ± 67.04
k (m^2)	$1.08 \cdot 10^{-18} \pm 9.83 \cdot 10^{-19}$	$4.56 \cdot 10^{-15} \pm 2.51 \cdot 10^{-15}$	$1.51 \cdot 10^{-18} \pm 4.08 \cdot 10^{-18}$	$2.01 \cdot 10^{-16} \pm 2.69 \cdot 10^{-16}$

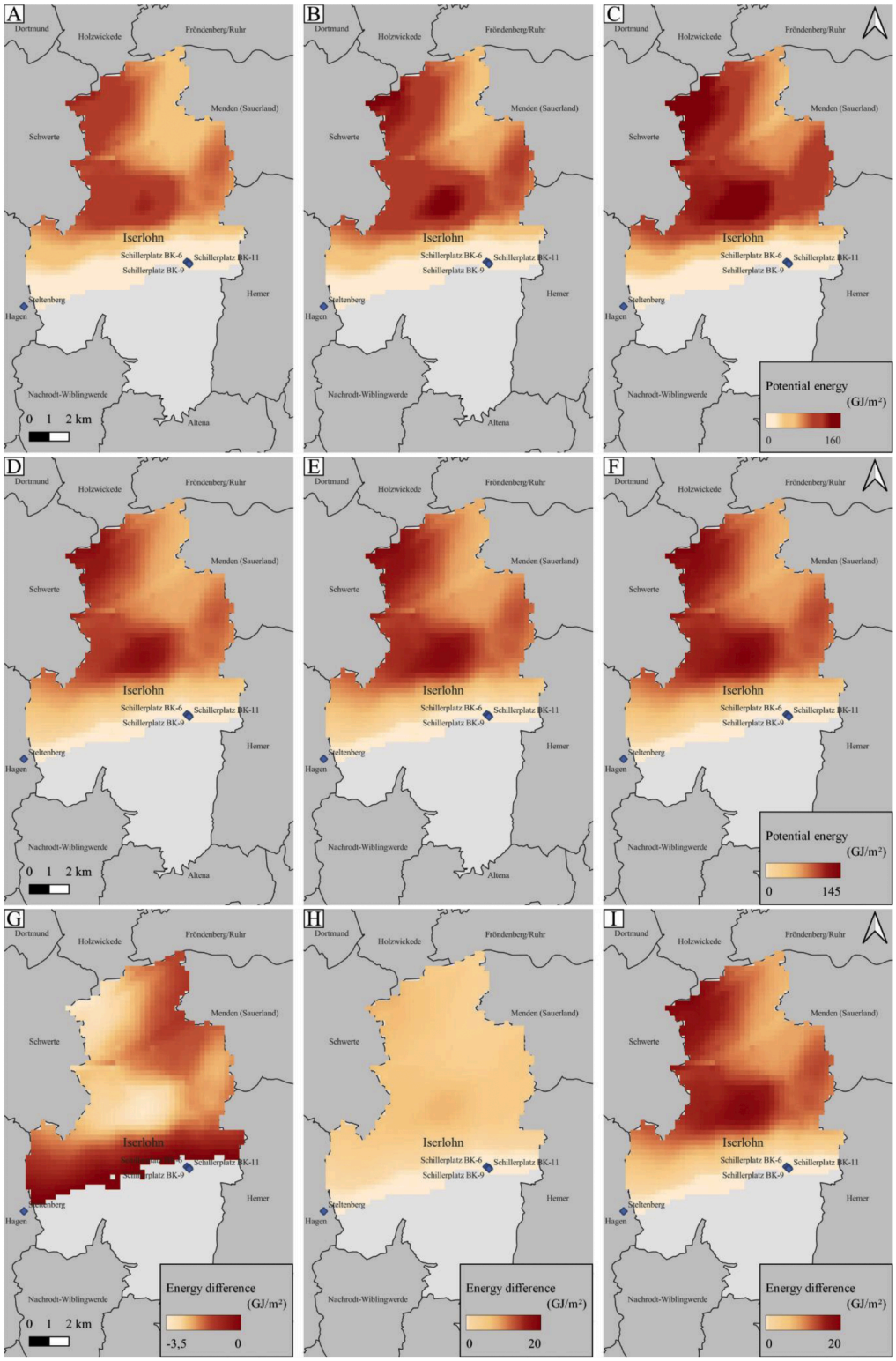

Fig. 10. Energy distribution of Devonian carbonates in Iserlohn. (**A**) displays the P90 percentile, (**B**) represents the distribution of the P50 percentile and (**C**) illustrates the least probable energy distribution of the P10 percentile of Devonian carbonates with high porosities of karstification. (**D**) displays the P90, (**E**) the P50 and (**F**) the P10 percentiles with only parameters of consolidated limestone and dolostone. (**G**) displays the P90, (**H**) the P50 and (**I**) the P10 energy difference between potentially karstified reservoir rocks and consolidated reservoirs. The location of the Steltenberg quarry and the three boreholes (BK-6, BK-9, and BK-11) from Iserlohn is indicated by blue diamonds.

Facies	Dolomitised Devonian limestone	Karstified carbonate	Hydrothermal dolostone
Rock type	Grainstone	Floatstone	Crystalline
Rock matrix	Micritic matrix	Micritic matrix	Dolomitic matrix
Mineralogy	Dolomite > calcite	Calcite + dedolomite	Dolomite >> Calcite
Porosity	Low: bound to fractures, microporosity	High: leaching, moldic, microporosity	Medium: vuggy and intercrystalline
Allochem content	Amphipora stromatopores, corals	Amphipora stromatopores, corals	Recrystallized fossils
Further features		Dedolomitization of the matrix, hydrothermal dolomite vein	
Drillcore scans	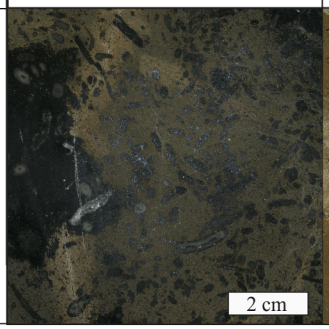	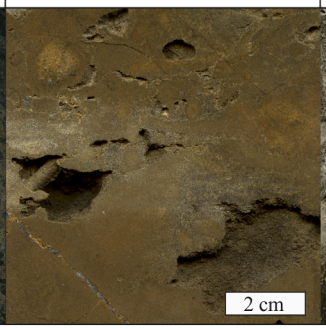	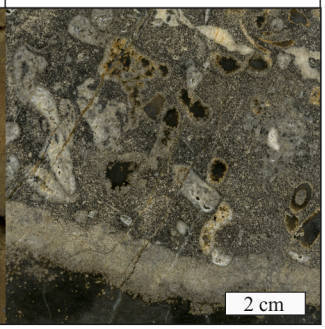

Fig. 11. Depositional and diagenetic facies in the Schillerplatz Drill-core. Dorp back-reef, karstified Dorp back-reef and hydrothermal dolostone. The depositional facies are applied following Krebs (1974), and the rock types were assigned after Dunham (1962) and Embry and Klovan (1971).

2010; Immenhauser, 2022; Mueller et al., 2024). This is supported by cathodoluminescence images, which display a patchy intrinsic luminescence in the radiaxial fibrous phase. All of these point to an oxidising porewater environment, whereby the precipitation probably extended into the shallow (marine) to intermediate marine burial domain (Ritter et al., 2015). This is evidenced by a cathodoluminescence transition from intrinsic luminescence to yellowish-orange luminescence, reflecting a shift from oxidising to reducing conditions (Ritter et al., 2015). Effects of deeper-seated, burial diagenetic processes are documented by dolograinstones and their paleothermometric/geochemical characteristics (Dol 1), which precipitated during subsequent burial approximately 381.4 ± 21.8/22.0 million years ago to approximately 6.5 km (Mueller et al., 2024). The former authors estimated the precipitation temperature of Dol 1 to be approximately 120–190 °C.

The partly dolomitic limestone later underwent fault-induced hydrothermal dolomitisation and subsequent dedolomitisation at depth, linked to folding and faulting during the Variscan Orogeny (Gillhaus et al., 2003). According to Mueller et al. (2024), the side strands of the Variscan thrust (striking WSW-ENE) near the Steltenberg quarry and in the Rhenish Slate Mountains formed pathways for Mg-rich hydrothermal fluids, which induced dolomitisation (Dol 2A and Dol 2B; Mueller et al., 2024). The presence of saddle dolomites (Dol 2B) suggests that formation temperatures ranging from 50 to over 200 °C, indicative of deep burial or hydrothermal formation conditions, occurred (Flügel, 2010; Zhang et al., 2025). In the Steltenberg quarry, Mueller et al. (2024) analysed the temperature of these saddle dolomites using microthermometry and clumped isotope thermometry, which indicated a temperature range of approximately 120–160 °C. These pathways were reactivated several million years later, causing corrosion and dissolution-reprecipitation, resulting in blocky calcites (LMC 1). Dedolomitised Variscan dolomites (Dedol 1) document a first dedolomitisation interval induced by corrosive hydrothermal/meteoric (mixed corrosion) fluids between the precipitation of Dol 2 and LMC 1. This process marks the earliest karstification horizon visible at Schillerplatz and, according to Mueller et al. (2024), reflects a shift in the fluid chemistry from Mg-saturated to undersaturated fluids (with respect to carbonate minerals).

A change in the regional stress field from WSW-ENE to NNW-SSE resulted in a post-Variscan geotectonic framework that induced large fault zones cross-cutting the Devonian units (Balcewicz et al., 2021; Mueller et al., 2024). During this period, several dissolution-reprecipitation phases occurred, including hypogenic and mixed-corrosion karstification, which resulted from far-field events in the Eurasian Plate (Mueller et al., 2024). Mineral phases related to this hydrothermal interval include the formation of a second blocky calcite phase (LMC 2) and the formation of dolomite Dol 3A and Dol 3B in the rocks studied here (Pederson et al., 2021; Mueller et al., 2024). Formation temperatures of Dol 3B were analysed by means of microthermometry and clumped isotope thermometry, yielding a result of 133 ± 34 °C (Mueller et al., 2024). The data support the interpretation, in agreement with Drozdzewski et al. (2017), that dolomitisation in Iserlohn is linked to regional fault zones, with a comparable setting found in

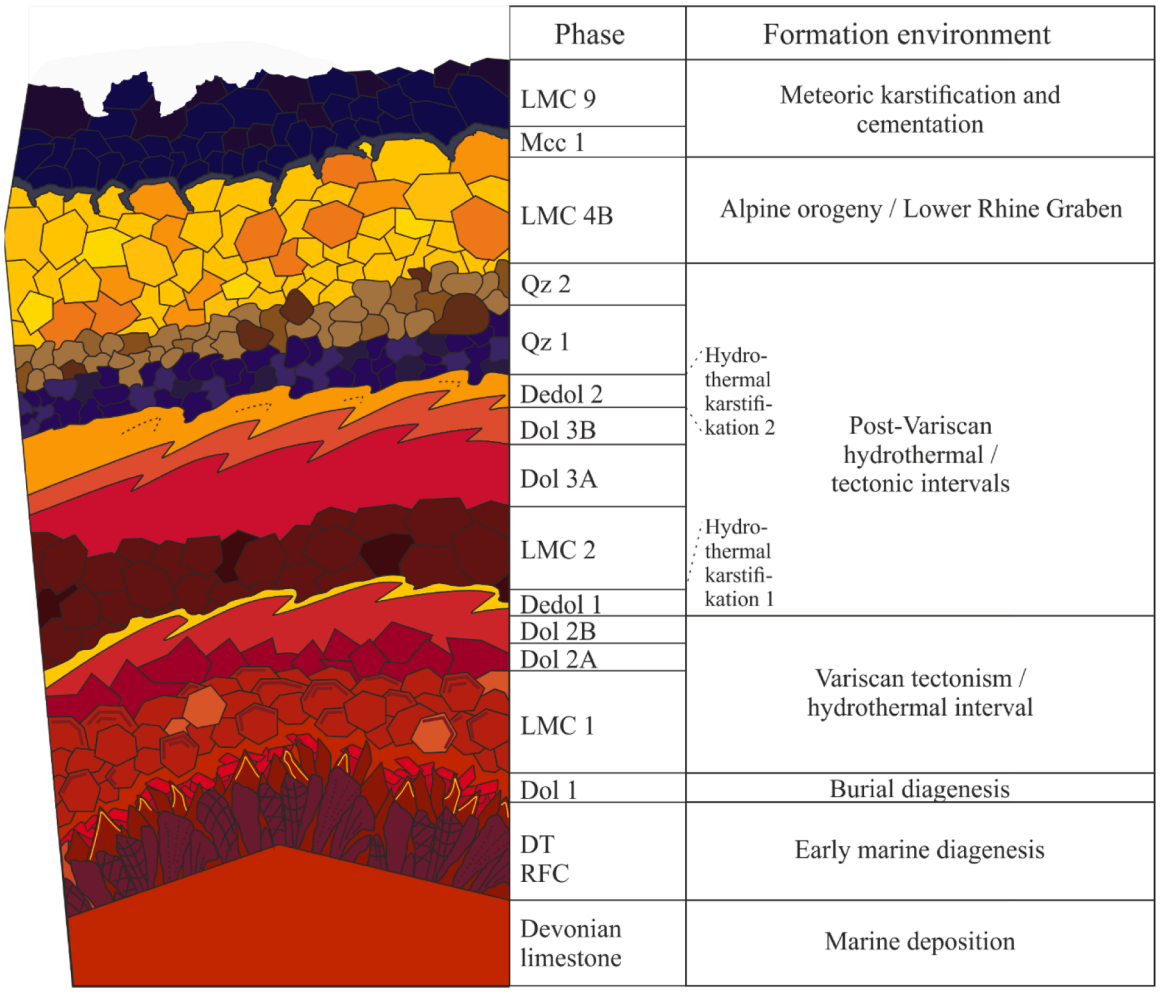

Fig. 12. Paragenetic sequence of the diagenetic phases in drill cores from Schillerplatz. The phases are coloured according to their cathodoluminescence and are therefore related to their precipitation environment. Tectonic activity phases and formation environments were compiled based on Mueller et al. (2024) and the references therein.

the nearby Hagen-Hohenlimburg area. Following Dol 3 precipitation, a second dedolomitisation stage (Dedol 2) occurred, possibly due to hypogenic karstification by corrosive fluids at depth. Mueller et al. (2024) also suggested that Dedol 2 may exhibit a meteoric karst signature, indicating fluid mixing at depth. Quartz cements (Qz 1 and Qz 2) precipitated in open pore space are attributed to renewed hydrothermal activity along post-Variscan fault zones (Mueller et al., 2024).

The latest stage of hydrothermal cement precipitation is assigned to the Alpine Orogeny (Mueller et al., 2024). During this period, large hydrothermal blocky calcites (LMC 4B) precipitated under temperature conditions of 94–110 °C (Mueller et al., 2024). The final calcite cement phases (Mcc 1 and LMC 9), characterised by typical intrinsic dark-blue luminescence, indicate an oxidising meteoric fluid environment (cf., Habermann et al., 1996; Neuser, 1988).

5.3. *Impact of karstification on the petrophysical and hydraulic properties*

The Devonian carbonate formations studied exhibit substantial heterogeneity in their petrophysical properties, which can be attributed to differences in lithofacies, mineralogy, and diagenetic overprint. Balcewicz et al. (2021) investigated fracture geometries and discontinuity patterns in Devonian limestones and dolomitic limestones. In contrast, previous work by Lippert et al. (2022) and Mueller et al. (2024) focused on depositional settings and diagenetic overprint, particularly the calcite–dolomite transformation, in relation to fluid flow behaviour. Lippert et al. (2022) further highlighted the spatial heterogeneity in matrix permeability and porosity distribution across different depofacies types. Building on this work, the present study explicitly includes karstified lithologies and quantifies their petrophysical behaviour under both ambient and reservoir-relevant conditions, extending previous classifications by adding structurally overprinted porosity types that significantly enhance permeability.

Laboratory measurements under ambient and simulated reservoir conditions confirm that karstified limestone, dolostone, and unaltered limestone can be distinguished primarily by their effective porosity and permeability, while bulk density, acoustic wave velocities, and thermal properties provide limited differentiation potential (Fig 7; Table 1). The effective porosity of karstified limestone samples reached up to 14 %, while permeability values are in the ranged of $<2.0 \times 10^{-16}$ m². These values surpass those of dolostones (~4.0 % porosity; $<1.0 \times 10^{-17}$ m² permeability) and unaltered limestones (~1.5 % porosity; $<10^{-18}$ m² permeability) by up to two orders of magnitude. The enhancement is attributed to well-developed solution voids and partially connected macropores, often exceeding the plug diameter locally. Even fractured limestone samples exhibited low porosity (~1.5 %), but showed permeabilities in the range of approximately 5×10^{-15} m² due to open, intersecting fracture planes. In contrast, dolostones, despite their promising porosity, reveal moderate hydraulic properties unless karstification or secondary fracturing occurs (Machel, 2004; Weides et al., 2013). These findings align with observations that effective

permeability in carbonate rocks is primarily controlled by connected secondary porosity rather than matrix properties alone (Lippert et al., 2022; Mueller et al., 2024).

To assess the stress-dependent behaviour of hydraulic parameters under realistic reservoir conditions, thermo-triaxial cell experiments were performed on two representative core samples: one dolostone and one karstified limestone specimen. In both cases, permeability declined with increasing effective pressure and further declined at elevated temperature of 100 °C (Fig 8). The compaction behaviour of the dolostone sample changed significantly once an effective pressure of about 50 MPa was exceeded (corresponding to about 1.5 to 2 km depth), which is consistent with the critical crack closure pressure (e.g. Walsh, 1965; Mavko and Nur, 1978; Zhang et al., 1990; Ahrens, 2020) determined in previous studies for dolomitic carbonates (Nicolas et al., 2016; Trippetta et al., 2017; Lippert et al., 2022). Beyond this threshold, compaction transitioned to a linear regime, indicating that most compliant cracks and voids had closed, and subsequent deformation predominantly affected the stiff matrix and voids. This behaviour implies a lower crack density in the dolostone and confirms its elevated mechanical stability, as also reported by Schmoker and Halley (1982) and Ehrenberg et al. (2006). Specific storage capacity remained comparatively stable throughout the pressure range, resulting in a progressive decline of hydraulic diffusivity with depth. Thermal loading resulted in a further reduction in permeability and diffusivity, likely due to pore closure caused by thermal expansion. By contrast, the karstified limestone sample exhibited significantly greater pressure sensitivity. Due to its large internal voids and the irregular surface morphology of solution cavities, the rubber sealing sleeve ruptured at around 50 MPa during pressurisation. As a result, no simulated reservoir conditions (depth $>$ 2 km) could be simulated on this sample, an experimental limitation common in the laboratory testing of highly heterogeneous rock samples, which will be discussed in more detail below. Nevertheless, the low-pressure results indicate the most promising enhanced hydraulic properties, attributable to solution-enlarged conduits and interconnected macrovoids. These findings emphasise that, while dolostones provide enhanced mechanical integrity and reduced porosity loss with increasing depth, karstified carbonates, if structurally connected at the reservoir scale, can offer significantly higher permeability. This is also evident from visual inspections of the μCT scans conducted (Fig 9).

Hydraulic diffusivity, defined as the ratio between hydraulic transport and storage (eq. (7)), systematically decreases with increasing burial depth (i.e., increasing effective pressure and temperature). Hence, reservoir performance under in-situ conditions is generally expected to be lower than what might be inferred from low-pressure laboratory measurements. Decreasing hydraulic diffusivity with depth is primarily governed by the pressure sensitivity of permeability, while specific storage remains relatively stable (Fig 8E, F). This discrepancy highlights that only a fraction of the total void volume contributes to fluid transport, as storage-relevant pores are largely pressure-insensitive (indicated by the pressure resistance of specific storage capacity). Of particular importance is the spatial configuration of void types: the interplay between transport-effective and storage-dominant porosity is highly dependent on the geometry, accessibility, and connectivity of karst-related structures. This relationship is vividly illustrated in the μCT images (Fig 9), which show the heterogeneous and localised nature of karst voids and their limited intersection with the plug volume. Consequently, even when overall porosity is high, permeability and diffusivity can remain low if major conduits are poorly connected or unfavourably oriented.

The interpretation of petrophysical data obtained from laboratory

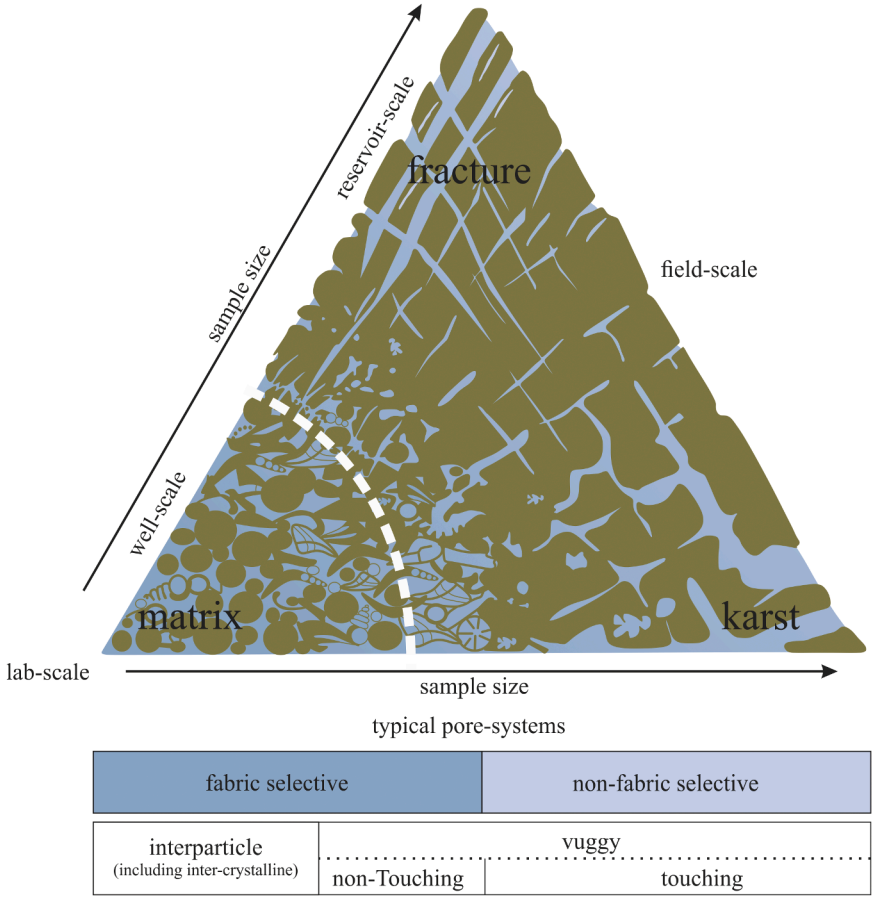

Fig. 13. Ternary diagram, showcasing the wide range of porosity components present in carbonate reservoirs, modified after Cross and Burchette (2025) and references therein.

core plugs must consider the inherent limitations of sample size and representativeness. Given the plugs' restricted dimensions, typically limited to a few centimetres, core plugs capture only a localised segment of the reservoir, often failing to represent its full heterogeneity (Fig 13; e.g., Clauser and Ernst, 1995; Guéguen et al., 1996; Geiger et al., 2010; Agar et al., 2013). This is particularly problematic in heterogeneous carbonate systems, where karst structures, solution cavities, and fracture networks frequently extend across scales several orders of magnitude larger than the sample itself. As a result, laboratory-determined permeability values, especially in karstified carbonates, should be regarded as conservative lower bounds of true formation-scale fluid flow. However, even whole-core analyses may fail to accurately represent the effective fluid-flow properties at the field scale (Cross and Burchette, 2025). Upscaling approaches that integrate geophysical imaging, borehole logging, hydrochemical profiling, and tracer tests are indispensable for predicting the real reservoir performance (e.g., Chesnaux et al., 2009). Ultimately, the successful exploitation of karstified geothermal reservoirs hinges on whether transmissive zones are not only present within the catchment area but also intersected by boreholes, an outcome that cannot be assumed without dedicated structural and hydrogeological investigation.

A further complication arises from the intrinsic variability of karstified and naturally fractured samples themselves. When solution-enlarged voids and fractures traverse the entire plug sample, the resulting measurements are highly sensitive to localised heterogeneities. No standardisation was applied in our study regarding the aperture width, cavity geometry, or presence of loose material in these voids (Fig 9). This methodological necessity reflects the natural variability of such systems. However, it also limits the reproducibility and comparability of individual measurements. Importantly, the matrix properties of these lithologies must not be neglected: even in strongly karstified samples, the bulk matrix contributes to overall mechanical and hydraulic behaviour and must be factored into any meaningful reservoir assessment.

5.4. Potential energy yield of Devonian carbonates in the study area

The quantification of uncertainty in geothermal resource assessments is challenging due to the dependence of input parameters on poorly characterised geological conditions. This hinders the application of probabilistic methods in evaluating geothermal resources. Consequently, the decision was made to utilise scarce petrophysical data, such as porosity, specific heat capacity, and density of the Devonian carbonates, to demonstrate the impact of geological uncertainty on resource base estimates.

Limitations of the modelled energy potential are found in the inhomogeneity of the lithology, due to the effects of (burial) diagenesis and erosion, such as karstification, petrophysical parameters can change significantly (Pederson et al., 2021; Lippert et al., 2022). The Monte Carlo simulation was necessary to represent the petrophysical reservoir properties due to the small sample quantity and the wide range of porosities, from low porosity limestone to high porosities of karstified carbonates. Furthermore, the specific heat capacity and density of the carbonates revealed significant variations in the laboratory measurements. While near-surface karstification is recognised as a potential cause of increased porosity and permeability in the upper hundreds of meters (Köhler, 1990; Ford and Williams, 2007; Drozdzewski et al., 2017), data for reservoir depths are lacking. Due to the absence of comprehensive data on karstification and other porosities, no weighting of the porosity distribution was applied.

The Aquifer thickness and temperature are further uncertainties, and this simulation relies on the thickness and heat model of Devonian carbonates in NRW provided by the Geologischer Dienst NRW (2023). Due to diagenesis affecting the Devonian carbonates (Gillhaus et al., 2003; Götte, 2004; Mueller et al., 2024), it is challenging to make a clear distinction between the least altered limestones, dolostones and possible karstification.

The potential energy yield of Iserlohn follows the trend of the input parameters, specifically the reservoir thickness and reservoir temperature. Accordingly, a higher potential energy yield was estimated for areas with a high thickness of the Devonian carbonates and high temperatures at reservoir depth. This observation is particularly evident in the central region of the Devonian carbonates in Iserlohn, where the thickness of the formations is notably substantial (reaching up to 800 m) and in the north-western sector, where the temperature is especially elevated, with recorded temperatures of up to 105 °C. In contrast, the energy yield in the southern part of Iserlohn is negligible due to the comparatively low temperatures of 10 °C and the minimal thicknesses, which can reach up to 270 m. Therefore, the potential energy stored in the subsurface is estimated to be higher, reaching up to 162 GJ per unit area in the southern part of Iserlohn, where the Devonian carbonates are at a greater thickness. Due to their deeper occurrence in the subsurface, the reservoir temperature is significantly increased.

A comparison between potentially karstified (Fig 10A–C) and a consolidated carbonate reservoir (Fig 10D–F) reveals that significant karstification locally increases the estimated energy potential. Within the P90 interval, the consolidated reservoir exhibits a marginally higher energy potential of up to 3.5 GJ/m^2 compared to the karstified scenario, driven by higher density and specific heat capacity. In contrast, the increased porosity in karstified samples tends to reduce the heat-in-place. At the P50 percentile, the karstified reservoir slightly exceeds the consolidated model by 5 GJ, whereas at the P10 percentile, karstification increases the energy potential by up to 13 GJ. It should be emphasised that the heat-in-place model does not consider permeability, which is essential for hydrothermal geothermal exploitation. Consequently, these results indicate a preference for geothermal systems not reliant on fluid flow in the subsurface (Ministerium für Umwelt, Landwirtschaft, Natur- und Verbraucherschutz des Landes Nordrhein-Westfalen, 2024).

5.5. Implications of karstification for geothermal reservoirs

Given the acknowledged value of enhanced permeability for geothermal reservoirs (Stober and Bucher, 2021), the natural pathways resulting from karstification present a promising precondition for the potential reservoir. The occurrence of karstification in carbonate rocks frequently leads to the formation of productive groundwater aquifers (Ribbert, 2012). As a karst-fissure aquifer, the Upper Jurassic (Malm) carbonates in Munich are the most significant reservoirs for geothermal utilisation in Central Europe (Goldscheider et al., 2010; Dirner and Steiner, 2015). The influence of facies- and diagenesis-controlled formations, as well as the resulting karstification on the hydraulic properties of the Malm, is considerable (Fritzer et al., 2012). The substantial geothermal usability of the Malm carbonates is attributed to the permeability of the formation, which is significantly influenced by karstification (Fritzer et al., 2012; Hofmann et al., 2014).

Devonian carbonates have also been investigated from the viewpoint of their suitability as geothermal reservoirs in many other places worldwide, for example, in the Alberta Basin, Canada. Comparable work to that of Lippert et al. (2022) for the Devonian of western Germany was conducted by Weydt et al. (2018) with a focus on the petrophysical properties of the Devonian carbonate matrix in Alberta. In the Alberta Basin, karstified Devonian carbonates show a permeability of 10^{-18} to 10^{-15} m^2 on a plug scale (Weydt et al., 2018), which is comparable to this studies results, where the permeability of the Iserlohn karstified carbonates is up to 10^{-16} m^2, showcasing a significant impact of karstification on the permeability compared to not karstified carbonates. A comparison of the matrix permeabilities investigated in the aforementioned studies revealed a high degree of similarity, with matrix permeabilities ranging from 10^{-19} to 10^{-18} m^2.

Laboratory measurements show a clear trend towards improved permeability in karstified carbonates, although the difficulty lies in the

scale. Larger features such as cavities (larger than the sample size), karstification or fracture zones cannot be represented, and an underestimated porosity or permeability of the outcrop or reservoir is likely to occur (Fig 13; Weydt et al., 2018; Cross and Burchette, 2025). Especially in carbonate reservoirs, porosity and permeability can vary significantly (Weydt et al., 2018). In instances where karstification networks may extend beyond the diameter of a sample plug, as is often the case in laboratory analyses, it is advisable to conduct well tests to ensure accurate results. These tests can serve to identify any excess permeability (Cross and Burchette, 2025).

The outcome is that Devonian carbonates are prone to substantial karstification, as described in previous studies (Köhler, 1990; Niggemann et al., 2008; Drozdzewski et al., 2017; Mueller et al., 2023, 2024; Jagert et al., 2025). The obtained paragenesis revealed that the karstification of the drill cores was caused by meteoric fluids, correlating with the meteorically precipitated carbonate cements described by Götte (2004) and Mueller et al. (2024). Thus, the analysed karst is considered to be meteoric karst in the sense of Klimchouk (2007). The crucial petrophysical parameters, such as porosity and permeability, are significantly improved in the measured karstified samples compared to the least altered limestones and dolostones. Despite this, the karstified samples appear to have a low permeability compared to the required permeabilities of 10^{-14} to 10^{-11} m² for hydrothermal utilisation (Moeck, 2014). Comparing the porosity and permeability results of Iserlohn to the play types classified by Moeck (2014), it appears, that the Devonian karstified carbonates plot as carbonate rock type I and not as karst dominated play (Fig 14). This is due to the fact that large karstification structures are not possible to be measured in the laboratory and only the improved trends are visible.

Whilst acknowledging the limitations of laboratory-scale experimentation, it is important to note that the underestimation of the permeability of the karstified samples from the Iserlohn cores can be attributed to the dimensions of the samples themselves. Given their substantial size, which exceeds the dimensions of the plugs utilised in laboratory experiments (80 mm in length and 40 mm in diameter), it is impractical to conduct experiments on larger karstification in a laboratory setting. An experimental study, involving a pumping test, was conducted by Jagert et al. (2025) at the Steltenberg quarry in Hagen-Hohenlimburg, near Iserlohn. The findings of this study indicate that the permeability of karstified Devonian carbonates in a borehole located near the surface can reach a maximum value of 3.6×10^{-13} m², which is significantly higher than the value found in laboratory analyses.

Overall, the Devonian carbonates exhibit considerable potential for hydrothermal geothermal development, as karstification can substantially increase both porosity and permeability. Variations in porosity and permeability also exert a decisive influence on advective heat transfer during fluid production and reinjection, since they govern both the effective heat exchange area and the geometry of fluid pathways. While higher porosity increases the interface area for thermal exchange (Heinze, 2024), the heat transfer coefficient is predominantly controlled by heat capacity, thermal conductivity, and, most importantly, flow velocity (Wakao et al., 1979). For geological materials, the dominance of velocity effects over intrinsic thermal properties has been demonstrated in several experimental studies (e.g., Gossler et al., 2020, and references therein). Yet, quantitative assessments of heat transfer coefficients in carbonate successions remain scarce, particularly for lithologies affected by karstification and associated macrovoid systems. This gap in data underscores the need for dedicated investigations targeting the interplay between karst-induced secondary porosity and heat transfer efficiency at reservoir conditions. Additionally, the fluid temperature at depth and the prognosed thickness of the reservoir, as reported by the Geologischer Dienst NRW (2023), and the resulting heat-in-place simulation reveal a significant potential energy yield across a wide area in Iserlohn. Nevertheless, further research is required to achieve a more precise understanding of the potential geothermal reservoir in Iserlohn, especially to provide new data on deep-seated hypogenic karstification. The formation of hypogenic karst is attributable to the presence of fluids, in which the aggressiveness has been produced at depth beneath the surface. This process occurs independently of surface or soil CO_2 or other near-surface acid sources. It is therefore not connected to meteoric karstification and occurs at intermediate to several kilometres in depth (Klimchouk, 2007). With no CO_2 input from the surface, the process of dissolution at depth can be renewed or enhanced by mixing waters of contrasting chemistry and dissolved gas content. This effect is widely referred to in the karst literature as "mixing corrosion" (Bögli, 1963;

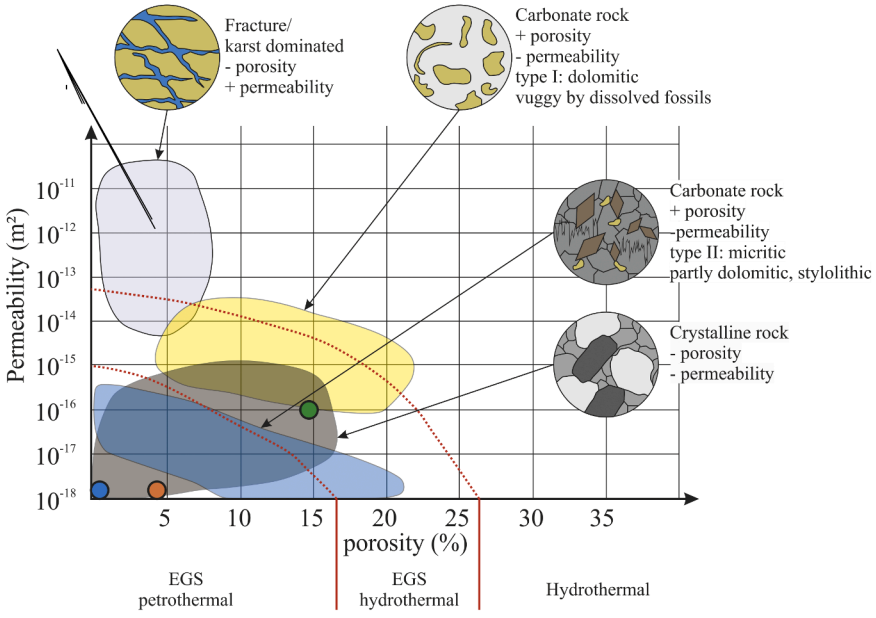

Fig. 14. Porosity and reservoir permeability plot, showcasing different reservoir types and potential geothermal systems. Values of carbonate rock type I reservoir originate from Upper Jurassic Malm carbonates of the Molasse Basin and carbonates from the Alberta Basin. Carbonate rock type II data originates from the Upper Jurassic of the Molasse Basin, data of fractured and karstified reservoirs stem from the Molasse Basin and the Alberta Basin and crystalline rock values were derived from the geothermal well Geretsried (Molasse Basin). Modified after Moeck et al. (2019) and references therein.

Klimchouk, 2007). Hydrothermal karstification encompasses hypogenetic karstification, where the corrosion of carbonates is triggered by the cooling of fluids along ascending flow paths (Dublyansky, 1995; Ford and Williams, 2007; Klimchouk, 2007). While measurements of epigenic karstification provide an initial insight into the enhanced porosity and permeability properties of Devonian carbonates, further studies on deeply karstified (hypogenic) carbonates are essential to assess the deeper reservoir properties.

6. Conclusions

This study offers important insights into the geothermal reservoir potential of karstified and fractured Devonian carbonates in Western Germany, highlighting both the significant promise and the challenges associated with their exploitation. The Devonian formations were originally buried to depths of 6.5 km but later uplifted and cooled, with 4 to 5.5 km of overlying material eroded from the overlying rocks. The investigation focused on three principal carbonate lithologies: non-karstified limestones, non-karstified dolostones, and karstified limestones and dolostones. These units are the fossil deposits of lagoonal or back-reef depositional environments, exhibiting pronounced lateral and stratigraphic heterogeneity influenced by structural and diagenetic processes. The reconstructed paragenetic sequence reflects successive periods of marine, burial, and meteoric diagenesis, with meteoric karstification exerting a particularly strong control on porosity and permeability. Evidence of hypogenic karstification related to deep-seated hydrothermal fluids is also observed, demonstrating the complex overprinting of karst processes during post-Variscan evolution.

Meteoric karstification was found to significantly enhance effective porosity, reaching up to 14 %, and permeability, up to 10^{-16} m^2, which are critical parameters for fluid flow in geothermal systems. Triaxial testing of karstified limestone under pressures of up to 50 MPa revealed that technical limitations prevented higher-pressure testing. In contrast, the dolostone samples exhibited notable changes in compaction behaviour at effective pressures of around 50 MPa, corresponding to depths of approximately 1.5 to 2 km. These results are consistent with the critical crack closure pressure, emphasising the influence of stress conditions on the hydraulic behaviour of deep carbonates. Thermo-triaxial experiments further suggest that increases in temperature and confining pressure have a more pronounced effect on transport properties than on storage capacities. Even at the laboratory scale, the impact of karst-induced secondary porosity and enhanced permeability is robust and significant, highlighting its exceptional nature.

Heat-in-place simulations were performed for both potentially karstified and consolidated reservoir scenarios in the study area. The spatially resolved model, covering 62,500 m^2, indicates that karstified reservoirs generally possess higher or comparable thermal energy content compared to consolidated carbonates. Within the P90 percentile, the consolidated reservoir exhibits a slightly higher energy potential due to its higher bulk density and specific heat capacity. In contrast, the higher porosity in karstified units locally reduces energy density. Conversely, at the P50 and P10 percentiles, karstified reservoirs display equal or higher energy potential, reflecting the interplay of heterogeneity, thickness, and reservoir temperature. These simulations demonstrate that variations in porosity, density, and specific heat capacity, as well as the degree of karstification, substantially influence the estimated heat-in-place, while permeability remains a critical factor for actual hydrothermal exploitation, particularly in fluid-driven systems.

The study highlights how geological complexity, particularly karstification, influences reservoir performance, while establishing a transferable framework for evaluating geothermal potential in analogous carbonate settings. These insights advance the understanding of Devonian carbonates in Western Germany and guide future geothermal exploration. Further research should aim to unravel the interplay between hypogenic carbonate dissolution at depth and subsequent meteoric karst overprinting during uplift, in order to refine predictions of reservoir behaviour and optimise geothermal exploitation strategies.

CRediT authorship contribution statement

Manfred Heinelt: Writing – original draft, Visualization, Methodology, Investigation, Formal analysis, Data curation. **Mathias Mueller:** Writing – original draft, Investigation, Data curation. **Benedikt Ahrens:** Writing – original draft, Visualization, Software, Methodology, Investigation, Data curation, Conceptualization. **Mathias Nehler:** Data curation. **Katharina Alms:** Software, Methodology. **Adrian Immenhauser:** Writing – original draft, Supervision, Project administration, Investigation.

Declaration of competing interest

The authors declare that they have no known competing financial interests or personal relationships that could have appeared to influence the work reported in this paper.

Acknowledgments

This project received funding from the Project Reallabor Geothermie Rheinland with Grant Number: 46SKD218X. We would like to thank Mathias Born, Tom Seemann, and Andreas Schulz (Ruhr-Universität Bochum) for preparing the thin sections. Furthermore, we would like to thank Hartmut Mammen (Ruhr-Universität Bochum) for carrying out the X-ray diffraction measurements. We would also like to thank René Hoffmann (Ruhr-Universität Bochum) for his assistance with the cathodoluminescence microscope, as well as Claudia Thoenes and Lucas Witte (Ruhr-Universität Bochum) for their help with sample preparation. The investigation of the drill core and acquisition of samples would not have been possible without the support of Dr. Tobias Fritschle, Martin Arndt, Sören Stichling, and Dr. Martin Salamon (Geologischer Dienst NRW); we would like to thank them as well.

Data availability

Data will be made available on request.

References

Agar, S., Geiger, S., Léonide, P., Lamarche, J., Bertotti, G., Gosselin, O., Hampson, G., Jackson, M., Jones, G., Kenter, J., Matthäi, S., Neilson, J., Pyrak-Nolte, L., Whitaker, F., 2013. Summary of the AAPG–SPE–SEG Hedberg Research conference on "fundamental controls on flow in carbonates. Am. Assoc. Pet. Geol. Bull 97, 533–552. https://doi.org/10.1306/12171212229.

Agemar, T., Schnellschmidt, R., Schulz, R., 2011. 3D-Modell der Untergrundtemperatur von Deutschland. Abstr. Proc. Geotherm. Boch.

Ahrens, B., Duda, M., Renner, J., 2018. Relations between hydraulic properties and ultrasonic velocities during brittle failure of a low-porosity sandstone in laboratory experiments. Geophys. J. Int 212, 627–645. https://doi.org/10.1093/gji/ggx419.

Ahrens, B., 2020. Experimental Analysis of the Frequency Dependence of Elastic and Hydraulic Properties of Fractured Rocks. Ruhr-Universität Bochum. Doctoral thesis.

Alms, K., Heinelt, M., Groeneweg, A., 2025. Lithium prospectivity and capacity assessment in Northern Germany. Geothermics 127, 103207. https://doi.org/10.1016/j.geothermics.2024.103207.

Arndt, M., 2021. 3D modelling of the Lower Carboniferous (Dinantian) as an indicator for the deep geothermal potential in North Rhine-Westphalia (NRW, Germany). ZDGG 172, 307–324. https://doi.org/10.1127/zdgg/2021/0279.

Balcewicz, M., Ahrens, B., Lippert, K., Saenger, E.H., 2021. Characterization of discontinuities in potential reservoir rocks for geothermal applications in the Rhine-Ruhr metropolitan area (Germany). Solid. Earth 12, 35–58. https://doi.org/10.5194/se-12-35-2021.

Becker, R.T., Aboussalam, Z.S., Stichling, S., May, A., 2016. The Givetian-Frasnian Hönne Valley Reef Complex (northern Sauerland) - an outline of stratigraphy and facies development. Münst. Forsch. Geol. Paläontol. 108, 126–140.

Bernabé, Y., Mok, U., Evans, B., 2006. A note on the oscillating flow method for measuring rock permeability. Int. J. Rock. Mech. Min. Sci. 43, 311–316. https://doi.org/10.1016/j.ijrmms.2005.04.013.

Blöcher, G., Kluge, C., Goense, T., Pei, T., Bakker, R.R., Bruhn, D., 2019. Hydraulic-mechanical Characterization of Geothermal Reservoir Rocks. Abstract European Geothermal Congress, 2019.

Bögli, A., 1963. Beitrag zur Entstehung von Karsthöhlen. Höhle 14, 63–68.

Bosak, P., Ford, D.C., Glazek, J., Horacek, I., 1989. Paleokarst. A systematic and Regional Review. Academia Publishing House of the Czechoslovak Academy of Sciences, Prague. Vol. 1726.
Burley, S.D., 1978. Cathodoluminescence (applied to the study of sedimentary rocks). In: Sedimentology. Encyclopedia of Earth Science (pp. 161–167). Springer, Berlin, Heidelberg, 1978. doi: 10.1007/978-1-4020-3609-5_37.
Burs, D., Bruckmann, J., Rüde, T.R., 2016. Developing a structural and conceptual model of a tectonically limited karst aquifer: a hydrogeological study of the Hastenrather Graben near Aachen. Ger. Env. Earth. Sci 75, 1253. https://doi.org/10.1007/s12665-016-6039-x.
Chesnaux, R., Allen, D.M., Jenni, S., 2009. Regional fracture network permeability using outcrop scale measurements. Eng. Geol. 108, 259–271. https://doi.org/10.1016/j.enggeo.2009.06.024.
Clauser, C., Ernst, H., 1995. Thermal conductivity of rocks and minerals. Rock. Phys. Ph. Relat. 3, 105–126.
Clostermann, M., 2018. Markscheiderisch-geotechnische Stellungnahme zur altbergbaulichen Situation innerhalb der Leistungsgrenze der Umgestaltung des Schillerplatzes in Iserlohn. Marks.-Geotech. Consult. Dortm. 25.
Coniglio, M., Frizzell, R.O.B., Pratt, B.R., 2004. Reef-capping laminites in the upper silurian carbonate-to-evaporite transition, Michigan Basin, south-western Ontario. Sedimentology 51, 653–668. https://doi.org/10.1111/j.1365-3091.2004.00641.x.
Cross, N.E., Burchette, T.P., 2025. Middle Eastern carbonate reservoirs – the critical impact of discrete zones of elevated permeability on reservoir performance. Geological Society, London. Spec. Publ. 548, 65–113. https://doi.org/10.1144/SP548-2023-144.
Darcy, H., 1856. Les Fontaines Publiques De La Ville De Dijon. Victor Dalmant, Paris.
DIN 18124:2019-02, 2019. Soil investigation and testing - determination of density of solid particles - wide mouth pycnometer.
Dirner, S., Steiner, U., 2015. Assessing reservoir uncertainty with stochastic facies modeling of a hydrothermal medium enthalpy reservoir (Upper Jurassic Carbonates of the Southern German Molasse Basin). Abstract Proceedings World Geothermal Congress 2015.
Drozdzewski, G., Richter, D.K., Wrede, V., 2017. Hydrothermalkarst Im nördlichen, Rheinischen Schiefergebirge. Munich, Verband der Deutschen Höhlen und Karstforscher e. V., München, 89 pp.
Dublyansky, Y.V., 1995. Speleogenetic history of the Hungarian hydrothermal karst. Environ. Geol. 25, 24–35. https://doi.org/10.1007/BF01061827.
Dunham, R.J., 1962. Classification of carbonate rocks according to depositional textures.
Ehrenberg, S.N., Eberli, G.P., Keramati, M., Moallemi, S.A., 2006. Porosity-permeability relationships in interlayered limestone-dolostone reservoirs. Bulletin 90, 91–114. https://doi.org/10.1306/08100505087.
Embry, A.F., Klovan, J.E., 1971. A late devonian reef tract on northeastern Banks Island, NWT. Bull. Can. Pet. Geol. 19, 730–781. https://doi.org/10.35767/gscpgbull.19.4.730.
Fischer, G.J., 1992. The determination of permeability and storage capacity: pore pressure oscillation method. In Evans, B., Wong, T.-F. (Eds.) Int. Geophys., 51, pp. 187–211. doi: 10.1016/S0074-6142(08)62823-5.
Flügel, E., 2010. Microfacies of Carbonate Rocks. Analysis, Interpretation and Application. Spinger, Berlin, Heidelberg, p. 996, 2nd ed.
Ford, D., Williams, P., 2007. Karst Hydrogeology and Geomorphology. John Wiley & Sons Ltd, West Sussex. https://doi.org/10.1002/9781118684986, 562 pp.
Fritschle, T., Strozyk, F., Oswald, T., Stubbe, H., Salamon, M., 2021. Deep geothermal energy potential at Weisweiler, Germany: exploring subsurface mid-palaeozoic carbonate reservoir rocks. ZDGG 172, 325–338. https://doi.org/10.1127/zdgg/2021/0292.
Fritzer, T., Pamer, R., Schulz, U., Sieblitz, S., 2012. Geothermische Charakterisierung von Karst-Kluft-Aquiferen im Großraum München, Endbericht. Bayer. Landesamt. Umw. 37.
Fritzer, T., Settles, E., Dorsch, K., 2022. Bayerischer Geothermieatlas-Hydrothermale Energiegewinnung. Bayerisches Staatsministerium für Wirtschaft,. Landesentwicklung und Energie, Munich, 138 pp.
Fryar, A.E., 2021. Groundwater of carbonate aquifers. In Mukherjee, A., Scanlon, B.R., Aureli, A., Langan, S., Guo, H., McKenzie, A.A., (Eds.), Global Groundwater (pp. 23–34) Elsevier. doi: 10.1016/B978-0-12-818172-0.00002-5.
Garland, J., Tucker, M., Scrutton, C., 1996. Microfacies analysis and metre-scale cyclicity in the Givetian back-reef sediments of south-east Devon. Proc,. Ussher. Soc 9, 31–36.
Geiger, S., Cortis, A., Birkholzer, J.T., 2010. Upscaling solute transport in naturally fractured porous media with the continuous time random walk method. Water. Resour. Res 46, 1–13. https://doi.org/10.1029/2010WR009133.
Geologischer Dienst NRW, 2023. Informationssystem Geothermie von Nordrhein-Westphalen, https://www.opengeodata.nrw.de/produkte/geologie/geologie/RK/ISGT, accessed: 07/31/2025.
Gillhaus, A., Götte, T., Richter, D.K., 2003. Polyphase spätdiagenetische Dolomitbildung im mittel- bis oberdevonischen Massenkalk von Hagen-Hohenlimburg (Remscheid-Altenaer Sattel,. Rhein. Schiefergebirge). Mitt,. Ges,. Geol,. Bergbaustud,. Österr 46, 51–66.
Goldscheider, N., Mádl-Szőnyi, J., Erőss, A., Schill, E., 2010. Review: thermal water resources in carbonate rock aquifers. Hydrogeol. J 18, 1303–1318. https://doi.org/10.1007/s10040-010-0611-3.
Gossler, M.A., Bayer, P., Rau, G.C., Einsiedl, F., Zosseder, K., 2020. On the limitations and implications of modeling heat transport in porous aquifers by assuming local thermal equilibrium. Water. Resour. Res 56 (10). https://doi.org/10.1029/2020WR027772 e2020WR027772.
Götte, T., 2004. Petrographische Und Geochemische Untersuchungen zu den postvariszischen Mineralisationen im devonischen Massenkalk des nordwestlichen rechtsrheinischen Schiefergebirges unter besonderer Berücksichtigung der Kathodolumineszenz. Doctoral thesis. Ruhr-Universität Bochum, Bochum. Institute of Geology, Mineralogy and Geophysics.
Grabert, H., 1998. Abriß der Geologie von Nordrhein-Westfalen. Schweizerbart, Stuttgart,, 351 pp.
Guéguen, Y., Gavrilenko, P., Le Ravalec, M., 1996. Scales of rock permeability. Surv. Geophys 17, 245–263. https://doi.org/10.1007/BF01904043.
Habermann, D., Neuser, R.D., Richter, D.K., 1996. REE-activated cathodoluminescence of calcite and dolomite: high-resolution spectrometric analysis of CL emission (HRS-CL). Sediment. Geol. 101, 1–7. https://doi.org/10.1016/0037-0738(95)00086-0.
Heinelt, M., Mueller, M., Ahrens, B., 2025, Karstic complexity in Geothermal Exploration: Petrophysical and Mineralogical Perspectives from Devonian Carbonates, Abstract 86th EAGE Annual Conference & Exhibition, Jun 2025. doi:10.3997/2214-4609.202510221.
Heinze, T., 2024. Multi-phase heat transfer in porous and fractured rock. Earth-Sci. Rev. 251, 104730. https://doi.org/10.1016/j.earscirev.2024.104730.
Hoek, E., Franklin, J.A., 1968. Simple triaxial cell for field or laboratory testing of rock. Trans. Inst. Min. Metall. 77, 22–26.
Hofmann, H., Blöcher, G., Börsing, N., Maronde, N., Pastrik, N., Zimmermann, G., 2014. Potential for enhanced geothermal systems in low-permeability limestones – stimulation strategies for the Western Malm karst (Bavaria). Geothermics 51, 351–367. https://doi.org/10.1016/j.geothermics.2014.03.003.
Hölting, B., Coldewey, W.G., 2013. Hydrogeologie: Einführung in die allgemeine Und angewandte Hydrogeologie. Springer, Berlin, Heidelberg, 438 pp.
Homuth, S., Götz, A.E., Sass, I., 2015. Reservoir characterization of the upper Jurassic geothermal target formations (Molasse Basin, Germany): role of thermofacies as exploration tool. Geoth. Energ. Sci 3, 41–49. https://doi.org/10.5194/gtes-3-41-2015.
Hörbrand, T., Beichel, K., Bendias, D., Savvatis, A., Kohl, T., 2025. Karst control on reservoir performance of a developed carbonate geothermal reservoir in Munich. Ger.,. SP 548, 291–310. https://doi.org/10.1144/SP548-2024-42.
Immenhauser, A., Dublyansky, Y.V., Verwer, K., Fleitman, D., Pashenko, S.E., 2007. Textural, elemental, and isotopic characteristics of pleistocene phreatic cave deposits (Jabal Madar, Oman). J. Sediment. Res. 77, 68–88. https://doi.org/10.2110/jsr.2007.012.
Immenhauser, A., 2022. On the delimitation of the carbonate burial realm. Depos. Rec. 8, 524–574. https://doi.org/10.1002/dep2.173.
Immenhauser, A., Hoffmann, R., Riechelmann, S., Mueller, M., Scholz, D., Voigt, S., Niggemann, S., Buhl, D., Dornseif, M., Platte, A., 2023. Petrographic and geochemical constraints on the formation of gravity-defying speleothems. Depos. Rec. 9, 413–436. https://doi.org/10.1002/dep2.199.
Immenhauser, A., Rameil, N., 2011. Interpretation of ancient epikarst features in carbonate successions — a note of caution. Sediment. Geol. 239, 1–9. https://doi.org/10.1016/j.sedgeo.2011.05.006.
Jagert, F., Kruszewski, M., Mueller, M., Wohnlich, S., Immenhauser, A., 2025. Aquifer characterisation of the karstified Massenkalk carbonates as potential geothermal reservoir: implications from borehole logging and hydraulic testing (Hagen, Germany). ZDGG 176, 95–114. https://doi.org/10.1127/zdgg/2025/0450.
James, N.P., Choquette, P.W., 1990. Limestone diagenesis, the meteoric environment. In McIlreath, I. and Morrow, D., (Eds.) Sediment Diagenesis (pp. 36–74). Geological Association Canada, Reprint Series 4.
Klimchouk, A., Palmer, A.N., De Waele, J., Auler, A.S., Audra, P., 2017. Hypogene Karst Regions and Caves of the World. Springer International Publishing,. https://doi.org/10.1007/978-3-319-53348-3, 911 pp,.
Klimchouk, A., 2007. Hypogene speleogenesis: Hydrogeological and Morphogenetic Perspective. National Cave and Karst Research Institute, Carlsbad,, 106 pp.
Koelen, K., Alber, M., Duda, M., Backers, T., 2021. Effect of sloppy sample preparation on results from uniaxial compressive strength tests. IOP. Conf. Ser.:. Earth. Environ. Sci. 833, 12030. https://doi.org/10.1088/1755-1315/833/1/012030.
Köhler, H.-J., 1990. Geologische und hydrogeologische Verhältnisse im Raum Gruiten-Dornap und Auswirkungen von Wasserhaltungsmaßnahmen in Steinbrüchen devonischer Massenkalke. Mitt. Ingenieurgeologie. Hydrogeol. 40, 198.
Kranz, R.L., Saltzman, J.S., Blacic, J.D., 1990. Hydraulic diffusivity measurements on laboratory rock samples using an oscillating pore pressure method. Int. J. Rock. Mech. Min. Sci. Geomech. Abstr. 27, 345–352. https://doi.org/10.1016/0148-9062(90)92709-N.
Krebs, W., 1967. Reef Development in the Devonian of the Eastern Rhenish Slate Mountains. CSPG Spec. Pub., Germany, 2, p. 295-306.
Krebs, W., 1968. Facies types in Devonian back-reef limestones in the Eastern Rhenish Schiefergebirge. In: Recent Developments in Carbonate Sedimentology in Central Europe. pp. 186–195. doi: 10.1007/978-3-662-40226-9.
Krebs, W., 1974. Devonian carbonate complexes of Central Europe. Bulletin 54, 155–208. https://doi.org/10.2110/pec.74.18.0155.
Land, L.S., 1970. Phreatic versus vadose meteoric diagenesis of limestones: evidence from a fossil water table. Sedimentology 14, 175–185. https://doi.org/10.1111/j.1365-3091.1970.tb00191.x.
Limberger, J., Boxem, T., Pluymaekers, M., Bruhn, D., Manzella, A., Calcagno, P., Beekman, F., Cloetingh, S., van Wees, J.D., 2018. Geothermal energy in deep aquifers: a global assessment of the resource base for direct heat utilization. Renew. Sustain. Energy. Rev. 82, 961–975. https://doi.org/10.1016/j.rser.2017.09.084.
Lippert, K., Ahrens, B., Nehler, M., Balcewicz, M., Mueller, M., Bracke, R., Immenhauser, A., 2022. Geothermal reservoir characterisation of Devonian carbonates in North Rhine-Westphalia (W. Germany): mineralogy- and depofacies-related extrapolation of petrophysical parameters. Geothermics 106, 102549. https://doi.org/10.1016/j.geothermics.2022.102549.

Littke, R., Büker, C., Hertle, M., Karg, H., Stroetmann-Heinen, V., Oncken, O., 2000. Heat flow evolution, subsidence and erosion in the Rheno-hercynian orogenic wedge of central Europe. SP 179, 231–255. https://doi.org/10.1144/GSL.SP.2000.179.01.15.
Löw, M., Söte, T., Becker, R.T., Stichling, S., May, A., Aboussalam, Z.S., Zoppe, S.F., 2022. The initial phase of the Hönne Valley Reef at Binolen (northern Rhenish Massif, Middle Devonian). Palaeobio. Palaeoenv 102, 573–612. https://doi.org/10.1007/s12549-022-00540-4.
Machel, H.G., 2004. Concepts and models of dolomitization: a critical reappraisal. SP 235, 7–63. https://doi.org/10.1144/GSL.SP.2004.235.01.02.
Manger, G.E., 1963. Porosity and bulk density of sedimentary rocks. Available online at https://pubs.usgs.gov/bul/1144e/report.pdf, accessed: 07/31/2025.
Marrero-Diaz, R., Ramalho, E., Costa, A., Ribeiro, L., Carvalho, J., Pinto, C., Rosa, D., Correia, A., 2015. Updated geothermal assessment of lower cretaceous aquifer in Lisbon Region, Portugal. Proceedings World Geothermal Congress 2015.
Marshall, D.J., 1988. Cathodoluminescence of Geological Materials. Academic division of Unwin Hyman Ltd, London,, 146 pp.
Mavko, G.M., Nur, A., 1978. The effect of nonelliptical cracks on the compressibility of rocks. J. Geophys,. Res 83, 4459–4468. https://doi.org/10.1029/JB083iB09p04459.
Moeck, I.S., 2014. Catalog of geothermal play types based on geologic controls. Renew. Sustain. Energy. Rev. 37, 867–882. https://doi.org/10.1016/j.rser.2014.05.032.
Moeck, I.S., Dussel, M., Weber, J., Schintgen, T., Wolfgramm, M., 2019. Geothermal play typing in Germany, case study Molasse Basin: a modern concept to categorise geothermal resources related to crustal permeability. Neth. J. Geosci. 98. https://doi.org/10.1017/njg.2019.12.
Mueller, M., Walter, B.F., Giebel, R.J., Beranoaguirre, A., Swart, P.K., Lu, C., Riechelmann, S., Immenhauser, A., 2024. Towards a better understanding of the geochemical proxy record of complex carbonate archives. Geochim. Cosmochim. Acta 376, 68–99. https://doi.org/10.1016/j.gca.2024.04.029.
Mueller, M., Heinelt, M., Walter, B.F., Beranoaguirre, A., 2025. The impact of diagenesis on rock properties in geothermal carbonate reservoirs. Abstract 86th EAGE Annual Conference & Exhibition, Jun 2025. doi: 10.3997/2214-4609.202510234.
Mueller, M., Walter, B.F., Beranoaguirre, A., Heinelt, M., Immenhauser, A., 2023. Hydrothermal karst cavities in a Devonian carbonate reservoir analogue (Rhenish Massif, Germany): implications for geothermal energy potential. Abstr. SEG. https://doi.org/10.59490/seg.2023.550, 2023.
Muffler, P., Cataldi, R., 1978. Methods for regional assessment of geothermal resources. Geothermics 7, 53–89. https://doi.org/10.1016/0375-6505(78)90002-0.
Ministerium für Umwelt, Landwirtschaft, Natur- und Verbraucherschutz des Landes Nordrhein-Westfalen, 2024. Masterplan Geothermie Langfassung. MWIKE NRW,, 56 pp.
Nehler, M., 2017. Evaluation of porosity and permeability estimates for rock samples based on X-ray micro-tomography. Doctoral thesis. Ruhr-Universität Bochum, Bochum. Institute of Geology, Mineralogy and Geophysics, 227 pp.
Neuser, R.D., Bruhn, F., Götze, J., Habermann, D., Richter, D.K., 1995. Kathodolumineszenz: Methodik und Anwendung. Zentralblatt. Geol. Paläontol., 287–306.
Neuser, R.D., 1988. Zementstratigraphie und Kathodolumineszenz des Korallenoolith (Malm) im südniedersächsischen Bergland. Boch. Geol. Geotech. Arb. 32, 1–172.
Nicolas, A., Fortin, J., Regnet, J.B., Dimanov, A., Guéguen, Y., 2016. Brittle and semi-brittle behaviours of a carbonate rock: influence of water and temperature. Geophys. J. Int 206, 438–456. https://doi.org/10.1093/gji/ggw154.
Niggemann, S., Richter, D.K., Voigt, S., Weber, H.-W., 2008. Karst und Höhlen im devonischen Massenkalk der Umgebung von Hagen/Iserlohn. Jahresber. Mitt. Oberrh. Geol. Ver. 90, 401–434. https://doi.org/10.1127/jmogv/90/2008/401.
Nöth, S., Karg, H., Littke, R., 2001. Reconstruction of late paleozoic heat flows and burial histories at the rhenohercynian-subvariscan boundary. Ger. Int. J. Earth. Sci. 90, 234–256. https://doi.org/10.1007/s005310000114.
Oncken, O., 1988. Aspects of the reconstruction of the stress history of a fold and thrust belt (Rhenish Massif, Federal Republic of Germany). Tectonophysics 152, 19–40. https://doi.org/10.1016/0040-1951(88)90027-3.
Paeckelmann, W., 1922. Der mitteldevonische Massenkalk des Bergischen Landes. Preuss. Geol. Landesanst., 1–365.
Pederson, C., Mueller, M., Lippert, K., Igbokwe, O.A., Riechelmann, S., Lersch, S., Benger, P., Verdeccia, A., Immenhauser, A., 2021. Impact of a regional fault zone on the properties of a deep geothermal carbonate reservoir unit (Devonian of NRW). ZDGG 172, 339–364. https://doi.org/10.1127/zdgg/2021/0281.
Popov, Y., Beardsmore, G., Clauser, C., Roy, S., 2016. ISRM suggested methods for determining thermal properties of rocks from laboratory tests at atmospheric pressure. Rock. Mech. Rock. Eng 49, 4179–4207. https://doi.org/10.1007/s00603-016-1070-5.
Popov, Y.A., Pribnow, D.F.C., Sass, J.H., Williams, C.F., Burkhardt, H., 1999. Characterization of rock thermal conductivity by high-resolution optical scanning. Geothermics 28, 253–276. https://doi.org/10.1016/S0375-6505(99)00007-3.
Ribbert, K.-H., 2012. Geologie Im Rheinischen Schiefergebirge. Bergisches Land. Geologischer Dienst NRW, Germany, Krefeld,, 194 pp.
Richter, D.K., Mueller, M., Platte, A., Scholz, D., 2020. Erste weichselzeitliche Kryocalcite im Attendorn-Elsper Riffkomplex (Frettermühler Wasserhöhle, Südwestfalen). Geol. Paläontol. Westphalen 93, 1–16.
Ritter, A.-C., Kluge, T., Berndt, J., Richter, D.K., John, C.M., Bodin, S., Immenhauser, A., 2015. Application of redox sensitive proxies and carbonate clumped isotopes to mesozoic and palaeozoic radiaxial fibrous calcite cements. Chem. Geol. 417, 306–321. https://doi.org/10.1016/j.chemgeo.2015.10.008.
Schepp, L.L., Ahrens, B., Balcewicz, M., Duda, M., Nehler, M., Osorno, M., Uribe, D., Steeb, H., Nigon, B., Stöckhert, F., 2020. Digital rock physics and laboratory considerations on a high-porosity volcanic rock. Sci. Rep 10, 5840. https://doi.org/10.1038/s41598-020-62741-1.
Schmoker, J.W., Halley, R.B., 1982. Carbonate porosity versus depth: a predictable relation for South Florida. Bulletin 66, 2561–2570. https://doi.org/10.1306/03B5AC73-16D1-11D7-8645000102C1865D.
Sepúlveda, J., Arancibia, G., Molina, E., Gilbert, J.P., Duda, M., Browning, J., Roquer, T., Morata, D., Ahrens, B., Bracke, R., 2020. Thermo-mechanical behavior of a granodiorite from the Liquiñe fractured geothermal system (39°S) in the Southern Volcanic Zone of the Andes. Geothermics 87, 101828. https://doi.org/10.1016/j.geothermics.2020.101828.
Sibley, D.F., Gregg, J.M., 1987. Classification of dolomite rock textures. J. Sediment. Res. 57, 967–975. https://doi.org/10.1306/212F8CBA-2B24-11D7-8648000102C1865D.
Stichling, S., Becker, R.T., Hartenfels, S., Aboussalam, Z.S., May, A., 2022. Drowning, extinction, and subsequent facies development of the Devonian Hönne Valley Reef (northern Rhenish Massif, Germany). Palaeobio. Palaeoenv. 102, 629–696. https://doi.org/10.1007/s12549-022-00539-x.
Stober, I., Bucher, K., 2021. Geothermal Energy. From Theoretical Models to Exploration and Development. Springer-Verlag, Berlin Heidelberg,. https://doi.org/10.1007/978-3-030-71685-1, 400 pp.
Trippetta, F., Carpenter, B.M., Mollo, S., Scuderi, M.M., Scarlato, P., Collettini, C., 2017. Physical and transport property variations within carbonate-bearing Fault zones: insights from the Monte Maggio Fault (Central Italy). Geochem. Geophys. Geosyst. 18, 4027–4042. https://doi.org/10.1002/2017GC007097.
Ufrecht, W., 2006. Zur Hydrogeologie der Aqifersysteme Buntsandstein und Muschelkalk zwischen Neckar und Donau. Schrifttenreihe des Amtes für Umweltschutz Stuttgart, 2006, 19–48.
Unger, T., Saillol, M., Aretz, M., Lokier, S., Mueller, M., Karius, V., Immenhauser, A., 2023. Inside a sediment-stressed Middle Devonian carpet reef: Cave exposes details of three-dimensional facies architecture and palaeoecology. Sedimentology 70, 1251–1280. https://doi.org/10.1111/sed.13078.
Uwakwe, O.C., Riechelmann, S., Mueller, M., Reinsch, T., Balcewicz, M., Igbokwe, O.A., Immenhauser, A., 2025. Scaling in fractured geothermal carbonate reservoir rocks: an experimental approach. Geothermics 125, 103199. https://doi.org/10.1016/j.geothermics.2024.103199.
Voland, V., Firsching, M., Müller, A., Mohr, S., Schön, T., Oeckl, S., Schröpfer, S., Hess, J., Habl, M., Freitag, J., Gruber, R., Uhlmann, N., 2010. Computed tomography (CT) system for automatic analysis of ice cores. https://www.ndt.net/article/ecndt2010/abstracts/3_05.pdf, accessed: 07/30/2025.
Wagner, W., 2009. Software For the Calculation of Thermodynamic Properties For a Great Number of Substances. FLUIDCAL. https://www.thermo.ruhr-uni-bochum.de/thermo/forschung/wagner_Fluidcal.html.en. accessed: 4/22/2025.
Wakao, N., Kaguei, S., Funazkri, T., 1979. Effect of fluid dispersion coefficients on particle-to-fluid heat transfer coefficients in packed beds: correlation of Nusselt numbers. Chem. Eng. Sci. 34 (3), 325–336. https://doi.org/10.1016/0009-2509(79)85064-2.
Walsh, J.B., 1965. The effect of cracks on the compressibility of rock. J. Geophys,. Res 70, 381–389. https://doi.org/10.1029/JZ070i002p00381.
Weides, S., Moeck, I., Majorowicz, J., Palombi, D., Grobe, M., 2013. Geothermal exploration of paleozoic formations in Central Alberta. Can,. J. Earth. Sci. 50, 519–534. https://doi.org/10.1139/cjes-2012-0137.
Weydt, L.M., Heldmann, C.-D.J., Machel, H.G., Sass, I., 2018. From oil field to geothermal reservoir: assessment for geothermal utilization of two regionally extensive Devonian carbonate aquifers in Alberta. Can. Solid. Earth 9, 953–983. https://doi.org/10.5194/se-9-953-2018.
Zhang, J., Wong, T.-F., Davis, D.M., 1990. Micromechanics of pressure-induced grain crushing in porous rocks. J. Geophys. Res 95, 341–352. https://doi.org/10.1029/JB095iB01p00341.
Zhang, Y.-F., Mueller, M., Hoffmann, R., Riechelmann, S., Chakraborty, S., Kaczmarek, S. E., Beyer, C., Immenhauser, A., 2025. Towards an improved understanding of Ca–Mg carbonates with nonplanar surfaces: an experimental approach. Sedimentology 72, 100–131. https://doi.org/10.1111/sed.13228.